Matter

Article

Low melting alkali-based molten salt electrolytes for solvent-free lithium-metal batteries

Solvent-free alkali molten salt electrolytes for LMBs

Non-volatility ✓ Low melting temperature ✓

Thermal stability ✓ Coulombic efficiency (>99%) ✓

Good ionic conductivity ✓ Al⁰ stability (>6 V) ✓

Minh Canh Vu, Priyadarshini Mirmira, Reginaldo J. Gomes, Peiyuan Ma, Emily S. Doyle, Hrishikesh S. Srinivasan, Chibueze V. Amanchukwu

chibueze@uchicago.edu

Highlights

Ternary alkali-based molten salts show low melting point and high conductivity

Molten salt electrolytes are oxidatively stable against aluminum up to 6 V

Molten salt electrolytes show improved compatibility with high voltage cathodes

Solvent-free molten salt electrolytes enable stable lithium-metal battery cycling

Lithium-metal batteries (LMBs) have shown promise in accelerating the electrification of transport due to high energy densities. Organic-solvent-based liquid electrolytes used in LMBs have high volatility and poor thermal stability. Safer solid polymer electrolytes suffer from low ionic conductivities, and inorganic solid-state conductors yield very resistive electrode/electrolyte interfaces. We report solvent-free, low-melting alkali salts that are nonvolatile and safe electrolytes with enhanced electrode/electrolyte interfaces, good conductivities, high oxidative stability, aluminum passivation, and long-term lithium-metal battery cycling with high-voltage cathodes.

Demonstrate
Proof-of-concept of performance with intended application/response

Matter

CellPress

Article

Low melting alkali-based molten salt electrolytes for solvent-free lithium-metal batteries

Minh Canh Vu,[1] Priyadarshini Mirmira,[1] Reginaldo J. Gomes,[1] Peiyuan Ma,[1] Emily S. Doyle,[1] Hrishikesh S. Srinivasan,[1] and Chibueze V. Amanchukwu[1,2,*]

SUMMARY

Developing advanced electrolytes is indispensable for next-generation lithium-metal batteries (LMBs). Unfortunately, the best electrolytes to date are volatile flammable liquids, which pose safety hazards, or solid-state inorganics, which have poor mechanical properties and resistive electrode/electrolyte interfaces. In this study, we report solvent-free inorganic molten salts—mixtures of alkali-based bis(fluorosulfonyl)amide salts—as electrolytes for LMBs that combine the nonvolatility and safety of solids with the improved electrode/electrolyte interfaces and conductivity of liquids. $Li_{0.3}K_{0.35}Cs_{0.35}FSA$ ternary molten salts with a low melting transition of ~45°C show higher conductivities and higher oxidative stabilities, support higher current densities, and have improved cycling compared to nonvolatile ionic liquids and solid-state polymer and inorganic conductors. They show excellent compatibility with both Li metal anodes (Coulombic efficiency ~99.8%) and high-voltage cathodes (no oxidation up to 6 V) without corrosion of the aluminum current collector. Solvent-free molten salt electrolytes provide a new class of electrolytes for a wide range of next-generation battery chemistries.

INTRODUCTION

The past three decades have seen tremendous growth in the use of portable electronics due to lithium-ion batteries.[1,2] However, as new applications such as electric vehicles grow, the specific energy of conventional Li-ion batteries may not keep pace with the need for higher energy density and lower costs.[3,4] Lithium-metal batteries (LMBs) have theoretical capacities that are an order of magnitude greater than graphite-based anodes in Li-ion batteries, and their low reduction potential coupled with conventional high-voltage cathodes can readily yield battery cells with overall cell voltages >4.5 V.[5,6] However, several challenges remain for wide-scale adoption. Lithium deposits in a dendritic manner that is dependent on factors such as electrolyte, current density, and pressure, among others,[7,8] and these dendrites further exacerbate parasitic reactions with the electrolyte. A compounding challenge that further doomed the first wave of LMB commercialization in the late 1980s was their propensity to explode, a safety hazard primarily attributed to the use of flammable electrolyte solvents.[9,10]

Several electrolyte design strategies have been explored to improve lithium metal's Coulombic efficiency (CE) (stripping capacity/deposition capacity),[11] such as by changing the solvent selection from conventional cyclic carbonates to ethers or fluorinated ethers.[12,13] However, volatility and flammability concerns remain. Increasing

PROGRESS AND POTENTIAL

Rechargeable lithium-metal batteries (LMBs) offer much higher energy densities, making them promising candidates for electric vehicle and grid storage applications. Conventional small-molecule electrolytes used in LMBs have high volatility and poor thermal stability. While ionic liquids (ILs) are less volatile, their bulky organic cations are vulnerable to degradation in LMBs, leading to reduced Coulombic efficiency and battery lifetimes. This work introduces a solvent-free, low-melting molten salt electrolyte for LMBs that is safer than state-of-the-art small molecules and more stable than IL electrolytes against Li metal. These molten salt electrolytes enable uniform Li deposition, high Coulombic efficiency, and wide electrochemical stability windows. Battery cycling with high-voltage cathodes shows that molten salts outperform ILs and volatile liquid electrolytes. This study highlights the potential of solvent-free molten salt electrolytes for safe and high-performance LMBs.

CellPress

salt concentration from conventional 1 M to higher values or using so-called localized high-concentration electrolytes (LHCEs) serves to significantly increase ion pairing and aggregate formation within the electrolyte.[14,15] These aggregates and ion pairs in high concentrated electrolytes decrease the fraction of "free solvent molecules" by ensuring that solvent molecules are bound in tight solvation shells with cationic and anionic species, thus preventing undesired solvent breakdown at both the anodic and cathodic interfaces.[16] The fluorination of ether to yield fluorinated ethers weakens the solvation ability of the ether and enhances ion pairing.[17] Hence, when lithium-metal deposition occurs, a lower overpotential is observed (ion desolvation barrier is decreased). More importantly, the interface is dominated by anion decomposition products.[18] It has been posited that these anion decomposition products lead to improved CEs and lithium-metal morphologies; hence, ion pairing has become a valuable descriptor. These observations have led to recent work on the design of new anions and solvents that can lead to ultrahigh salt concentrations.[19] Our guiding hypothesis becomes the following: if ion pairing and aggregate formation and an anion-dominated solid-electrolyte interphase (SEI) are so vital for LMBs, shouldn't we eliminate the solvent?

The conventional design strategy for an electrolyte involves a lithium salt dissolved in a solvent. While the solvent types (carbonate[20] vs. ether[21]) or phases (small molecule[22] vs. liquefied gas[23] vs. polymer[24]) or salt concentration[25] may change, the convention remains. Beyond improving the LMB performance with significant ion pairing, the elimination of solvent also addresses the volatility, flammability, and safety hazards that are even more crucial for LMBs. Molten-salt-based electrolytes consist solely of cations and anions and do not have solvents present.[26] As a result, they are nonvolatile and nonflammable and have high thermal stability.[27] A familiar class of molten salts are ionic liquid (IL) electrolytes, which are liquid at ambient conditions due to the weak interaction between their bulky organic cationic group and a delocalized anion.[28] Due to their low melting temperatures, they have been explored for LMBs as solvents for conventional salt-in-solvent electrolytes.[29,30] However, they have low lithium transference numbers, corrode the aluminum current collector,[31] lead to dendritic lithium deposits, and suffer from low CE, and the cations participate in similar decomposition reactions (e.g., elimination, hydrogen abstraction) to organic solvents, making ILs incompatible with lithium metal.[32]

In contrast to conventional/state-of-the-art ILs ("organic molten salts"), there exists a class of inorganic ILs ("molten salts") that provides a pathway to solving the challenges facing conventional ILs and organic solvents.[33] Here, only inorganic cations (such as Li^+, K^+, etc.) are present and are coupled with inorganic anions. Their often-higher melting transitions coupled with the low melting transition of lithium metal ($\sim$180°C) have led to fewer studies for lithium-based batteries. Inorganic ILs—or simply molten salts—can have lower melting transitions through either the design of an asymmetric and/or soft anion or through the formation of eutectics. For example, $LiNO_3/KNO_3$ eutectic molten salts are state of the art for lithium-air batteries.[34,35] However, their high eutectic melting point (125°C) leads to high battery operating temperatures of $\sim$150°C (only 30°C lower than the lithium-metal melting point), and a thick glass fiber separator or a solid-state conductor such as LAGP ($Li_{1.5}Al_{0.5}Ge_{1.5}P_3O_{12}$)[36] is needed, as conventional Celgard separators shrink at those temperatures,[37] limiting energy density.

Molten salts with soft anions based on the bis(fluorosulfonyl)amide (MFSA) and perfluorosulfonylamide (MPFSA) families can yield low melting transitions that rival conventional organic ILs.[38] Matsumoto et al. has shown these salts to have a strikingly

[1]Pritzker School of Molecular Engineering, University of Chicago, Chicago, IL 60637, USA

[2]Lead contact

*Correspondence: chibueze@uchicago.edu

https://doi.org/10.1016/j.matt.2023.10.017

CellPress

low melting point either through exploiting anionic asymmetry,[39,40] anionic size,[41] or Li/K/Cs-based eutectics.[38] Some have explored these for Li-ion batteries,[42] but no enhancement was obtained compared to traditional electrolytes. During the writing of this article, Wang et al.[43] reported the utilization of a different molten salt electrolyte composition for high-temperature LMBs. However, studying low-melting molten salts as electrolytes for LMBs is still underexplored.

Herein, we report that molten salt electrolytes with low eutectic melting temperatures ($\sim$45°C) can enable the operation of LMBs at moderate temperatures of 80°C–100°C. Lithium, potassium, and cesium salts with the bis(fluorosulfonyl)amide anion (LiFSA, KFSA, and CsFSA, respectively) were utilized to prepare binary ($Li_{0.45}K_{0.55}FSA$, 45:55, mol %) and ternary ($Li_{0.30}K_{0.35}Cs_{0.35}FSA$, 30:35:35, mol %) mixtures with relatively high ionic conductivities, high lithium transference numbers, wide electrochemical stability windows, and high CEs. We primarily exploit the fact that for molten salts, K and Cs (unlike sodium) deposit at potentials more negative than that for lithium. Therefore, when explored in LMBs, they lead to excellent lithium-metal deposition morphologies and enable reversible lithium-metal plating and stripping. Furthermore, they support long-term lithium-metal cycling with high-voltage $LiNi_{0.8}Mn_{0.1}Co_{0.1}O_2$ (NMC811) cathodes. When compared to typical state-of-the-art liquid electrolytes (1 M LiFSA/DME [1,2-dimethoxyethane]), they exhibit similar lithium-metal overpotentials (despite the lower viscosity and higher conductivity of liquid electrolytes) but enable improved cycling (Figure 1A; Table S1). When compared to nonvolatile ILs (1 M LiFSA/$Pyr_{14}FSA$ [1-butyl-1-methylpyrrolidinium bis(fluorosulfonyl)amide]), polymer, and inorganic solid-state electrolytes, these molten salts support higher current densities, higher ionic conductivities, and much improved cycling (Figure 1B; Table S2). Hence, inorganic molten salt electrolytes allow for the benefits of liquid electrolytes (faster ion transport and improved electrode/electrolyte interface) while retaining the desirable properties of solid electrolytes (nonvolatility, nonflammability). Our work introduces a solvent-free, low-melting molten salt electrolyte for the development of high-energy-density LMBs.

RESULTS AND DISCUSSION

Physicochemical and thermal properties of the alkali-based molten salts

Alkali salt mixtures (LiFSA, KFSA, and CsFSA) with different mole ratios were prepared, and their thermal and ionic conductivity properties were characterized. Since our focus is on enabling lithium-metal electrodeposition, we chose co-cations such as K^+ and Cs^+ that will not electrodeposit at potentials higher than the standard reduction potential of lithium in MFSA molten salt electrolytes.[44] Differential scanning calorimetry (DSC) was first utilized to determine the melting transition of the pristine salts and binary and ternary mixtures. Figure S1 shows the DSC thermograms of the salts and the mixtures chosen for the work. The single salts of LiFSA, KFSA, and CsFSA show peaks of the melting transitions (T_ms) of 142°C, 101°C, and 104°C, respectively, in agreement with others.[38] Figure 1C shows that binary and ternary mixtures of these salts have much lower T_m compared to single salts with near-equimolar binary $Li_{0.45}K_{0.55}FSA$ and $Li_{0.5}Cs_{0.5}FSA$ with T_ms of $\sim$68°C and 62°C, respectively, and the ternary $Li_{0.30}K_{0.35}Cs_{0.35}FSA$ exhibits an even lower eutectic T_m of $\sim$45°C (melting peak). The ternary onset T_m is about 33°C, similar to previous reports.[38,45] (Figure S1). The lower T_m of the ternary mixtures compared to the binary mixture may be attributed to changed electrostatic cation-anion interactions, as well as an increase in entropy, upon the introduction of CsFSA to the LiKFSA binary mixture. It is worth noting that the ratio with the lowest enthalpy of melting (ΔH_m) is not the ratio with the lowest melting point (Figures 1C and 1D).
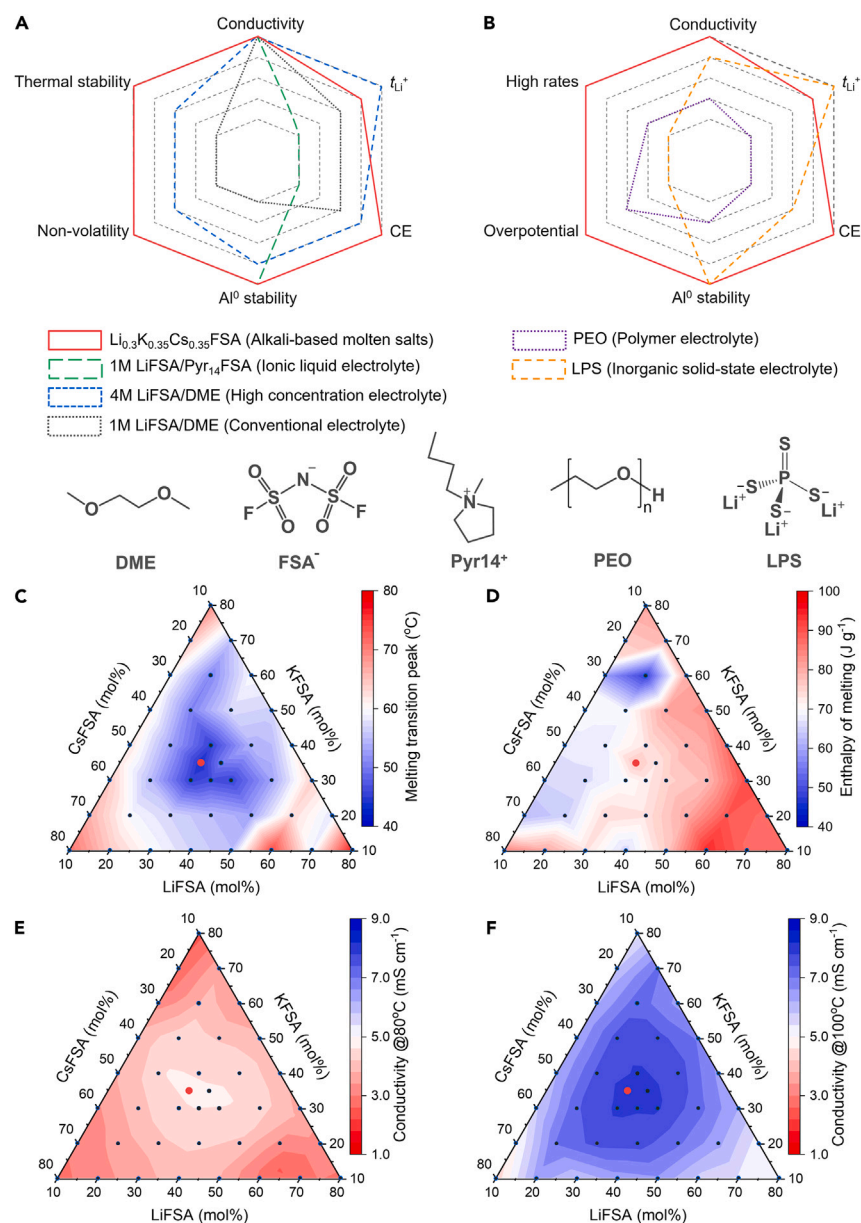
Figure 1. Overview and physiochemical properties

(A) A comparison of conventional electrolytes (e.g., 1 M LiFSA/DME), high-concentration electrolytes (e.g., 4M LiFSA/DME), organic ionic liquid electrolytes (e.g., 1 M LiFSA/Pyr$_{14}$FSA), and solvent-free molten salt electrolytes (Li$_{0.30}$K$_{0.35}$Cs$_{0.35}$FSA).

(B) A comparison of polymer electrolyte (PE), inorganic solid-state electrolyte (ISSE), and solvent-free molten salt electrolytes (Li$_{0.30}$K$_{0.35}$Cs$_{0.35}$FSA). Note that the properties of liquid electrolytes and IL electrolytes were measured at room temperature, while those of the PE and ISSE were measured at 60°C and the molten salt electrolytes at 80°C. Chemical structures of the relevant electrolytes are shown.

(C–F) Ternary diagrams of (C) melting point, (D) enthalpy of the melting transition, and (E and F) ionic conductivity of the low-melting molten salts at 80°C and 100°C, respectively, as a function of the salt molar fractions. The dots represent compositions where data were collected, with the red dot indicating the eutectic point of the ternary Li$_{0.3}$K$_{0.35}$Cs$_{0.35}$FSA molten salt. The color scale shows blue as desired and red as undesired. CE, Coulombic efficiency; t_{Li+}, lithium transference number; LPS, Li$_3$PS$_4$.

Matter
Article

CellPress

Further spectroscopic and computational studies beyond the scope of this study is warranted to further investigate these effects. The ternary eutectic mixture of $LiNO_3$–KNO_2–$CsNO_3$ has also been reported to have a T_m of $\sim$90°C, which is lower than the binary mixture ($LiNO_3$–KNO_3, 125°C).[34] Integrating the T_m peak area allows us to extract ΔH_m.[46] Figure 1D shows an average enthalpy in the range of 50–90 J g^{-1}, with higher amounts of LiFSA resulting in a greater ΔH_m. The $Li_{0.30}K_{0.35}Cs_{0.35}FSA$ mixture reached an enthalpy of roughly 55 J g^{-1}, which is significantly lower than the value for the binary of $LiNO_3$–KNO_3 nitrate salts ($\sim$130 J g^{-1}),[34] alkali-ternary nitrate salts (90–220 J g^{-1}),[47] and the pure pyrrolidinium-based bis(trifluorosulfonyl) imide ILs (134 J g^{-1}).[48] The low ΔH_m of the molten salts indicates weak intermolecular binding forces.

The ionic conductivity of the binary and ternary salts was measured using electrochemical impedance spectroscopy (EIS). Figures 1E and 1F show the ionic conductivity of the molten salts at 80°C and 100°C, respectively. We specifically focus on the temperatures of 80°C and 100°C, as they allowed for at least a $\sim$30°C temperature differential when compared to the T_m. In general, the lower the melting point of the molten salt mixtures, the higher the ionic conductivity, with ionic conductivities on the order 1 mS cm^{-1} above 60°C. Furthermore, the ionic conductivities of the $Li_{0.45}K_{0.55}FSA$ binary and $Li_{0.30}K_{0.35}Cs_{0.35}FSA$ ternary mixtures were also measured at a wide temperature range of 20°C–120°C (Figure S2), with the $Li_{0.45}K_{0.55}FSA$ binary mixture ($\sim$3.26 mS cm^{-1} at 80°C) exhibiting a lower ionic conductivity compared to that of the $Li_{0.30}K_{0.35}Cs_{0.35}FSA$ ternary mixture ($\sim$5.64 mS cm^{-1} at 80°C). The good ionic conductivity of the ternary molten salts can be attributed to the lower viscosity arising from the lower melting point. The binary mixture also exhibits a higher activation energy barrier than the ternary mixture (0.71 vs. 0.65 eV). Additionally, the lithium transference numbers (LTNs) of $Li_{0.45}K_{0.55}FSA$ and $Li_{0.30}K_{0.35}Cs_{0.35}FSA$ were determined via the Bruce-Vincent method[49] to be 0.39 and 0.48 at 80°C, respectively (Figure S3). This is significantly higher than the LTNs in IL electrolytes[50] (e.g., 1 M LiFSA/$Pyr_{14}FSA$, 0.1), polymer electrolytes[51] (e.g., 1 M LiTFSI/PEO, 0.2), and alkali nitrate molten salts[34] ($LiNO_3$–KNO_2–$CsNO_3$, 0.28) and is slightly higher than the LTN in fluorinated-ether-based liquid electrolytes (0.3–0.4).[12,52,53]

Electrochemical properties and interfacial behavior

The electrochemical properties of the molten salts were investigated using a suite of electrochemical and spectroscopic techniques. The binary $Li_{0.45}K_{0.55}FSA$ and ternary $Li_{0.30}K_{0.35}Cs_{0.35}FSA$ salt mixtures were selected due to their low melting points and acceptably high ionic conductivities and were characterized at 80°C and 100°C. For comparison at high temperature, the electrochemical properties of a nonvolatile IL electrolyte (1 M LiFSA/$Pyr_{14}FSA$) were also determined. Figure 2A shows the cyclic voltammograms (CVs) of our chosen molten salt electrolytes in Li||SS (stainless steel spacer) cells with a scan rate of 1 mV s^{-1} at 80°C. The CVs indicate that the molten salt electrolytes can support reversible plating and stripping of lithium metal at 0 V (vs. Li/Li^+). A 25 mV overpotential is observed that is quite similar to the 31 mV observed in the state-of-the-art liquid electrolyte 1 M LiFSA in FDMB (2,2,3,3-tetrafluoro-1,4-dimethoxybutane).[12] All voltages reported are vs. Li/Li^+ unless otherwise stated. Even though the reductive potentials of alkali metals in aqueous solution (Li: $-$3.045 V, K: $-$2.925 V, Cs: $-$2.923 V vs. standard hydrogen electrode [SHE]) are relatively close, Zhang and co-workers have demonstrated that only Li deposits, and no alloy of Li with other alkali metals (K, Cs, Rb), are formed in nonaqueous electrolytes.[54,55] Furthermore, we must note that alkali deposition potentials are dependent on the "solvent" media, with different solvents[56] or molten
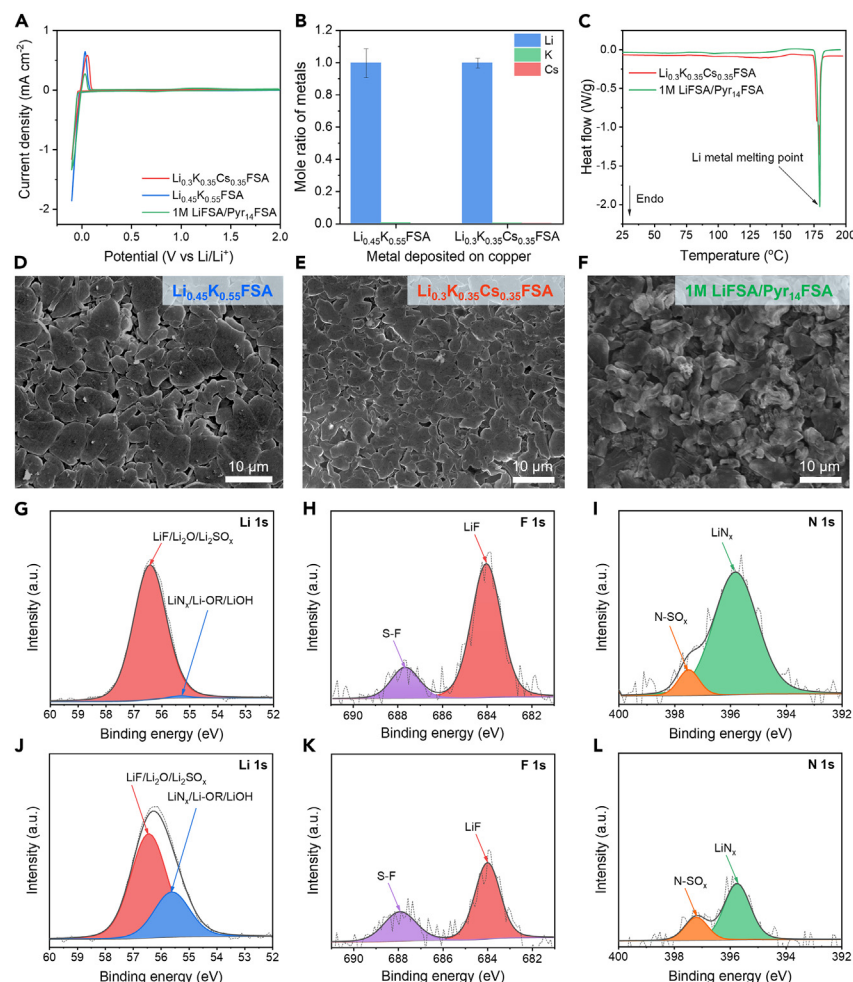
Figure 2. Lithium deposition

(A) CV profiles in Li‖SS half cells using molten salts and IL electrolytes at 80°C, at 1 mV s^{-1}.

(B) ICP-MS analysis of the metal layer deposited on copper electrodes in Li‖Cu half cells.

(C) DSC analysis of the metal layer deposited on copper electrodes in Li‖Cu half cells.

(D–F) SEM images showing the morphology of Li deposited on copper electrodes using (D) $Li_{0.45}K_{0.55}FSA$ electrolytes, (E) $Li_{0.30}K_{0.35}Cs_{0.35}FSA$, and (F) 1 M $LiFSA/Pyr_{14}FSA$ at 0.5 mA cm^{-2} for 1 mAh cm^{-2}, respectively.

(G–L) Deconvoluted XPS spectra of (G) Li 1s, (H) F 1s, and (I) N 1s of Li surface in Li‖Cu cells using $Li_{0.30}K_{0.35}Cs_{0.35}FSA$ molten salt electrolyte and of (J) Li 1s, (K) F 1s, and (L) N 1s of Li surface in Li‖Cu cells using 1 M $LiFSA/Pyr_{14}FSA$ electrolyte after 10 cycles, respectively. a.u., arbitrary units.

salts[44] affecting the relative order of deposition. To confirm that only Li is deposited, the elemental components of the deposited layer on copper electrodes were measured using inductively coupled plasma mass spectrometry (ICP-MS). Figure 2B shows that the composition of the deposits is primarily Li (>99%), while a minor amount of K and Cs and other metals can be observed due to residual salts and impurities. In addition, the electrolyte composition after cycling was quantified (Figure S4), with no change observed after metal deposition. Furthermore, the thermogram of the deposited metal on copper shows that there is a T_m peak at 180°C (close to the T_m of Li metal), while peaks for K (63.5°C) and Cs (28°C) are not observed (Figure 2C). We also electrodeposited metal using the ternary mixture of $Li_{0.3}Na_{0.35}K_{0.35}FSA$ electrolytes (Figure S4), where a melting peak can be observed

Matter
Article

CellPress

at ~98°C for Na metal, while another peak is centered at 163°C for the separator. This demonstrates that there is no deposition of Li when Na salt is used in the molten salt electrolyte.

The morphology of Li deposits on copper electrodes was also examined at different current densities and capacities at 80°C using scanning electron microscopy (SEM) (Figures 2D, 2E, and S5). With the binary $Li_{0.45}K_{0.55}FSA$ electrolytes, porous and fibrous morphologies of Li deposits can be observed at a current density of 0.5 mA cm^{-2} with a low capacity of 0.5 mAh cm^{-2} (Figure S5), while the cells with capacities of 1 (Figure 2D) and 2 mAh cm^{-2} (Figure S5) display deposits of compact aggregates of large nodule-like Li particles. In contrast, cells using the ternary electrolytes at a current density of 0.5 mA cm^{-2} at all tested capacities from 0.5 to 2 mAh cm^{-2} depict a dense nodule-like structure of deposited Li particles (Figures 2E and S5), which is similar to that of superior liquid electrolytes, e.g., 1 M LiFSA/FDMB.[12] We note that the smooth and compact Li deposit using the molten salt electrolyte may also be due to the so-called "self-healing electrostatic shield" (SHES) effect caused by additive cations such as Cs.[54–56] Interestingly, the Li deposits using the IL electrolyte (1 M LiFSA/Pyr$_{14}$FSA) show a rough and nonuniform surface due to the formation of whisker-shaped Li deposits (Figure 2F). Formation of high-density, low-surface-area nodule-like Li deposits of large particle size can help limit parasitic interfacial reactions with electrolytes and thus lead to high CE, improved cycle life, and better safety.[57] X-ray photoelectron spectroscopy (XPS) analysis was performed to reveal the chemical compositions of the interphase formed on the Li-metal surface in different electrolytes (Figures 2G–2L and S5). There are higher intensities of LiF (at 56.6 and 684 eV in Li 1s and F 1s spectra, respectively) and LiN_x (at 395.4 eV in N 1s spectra) in the interphase using molten salt compared to that of the IL electrolyte, while a higher intensity of the Li coupled with oxygen bonding (LiOH/LiOR/LiN_x) at 55.8 eV can be found in the interphase using the IL electrolyte with organic cations. Significant ion pairing between Li and FSA in the molten salt leads to FSA's presence at the Li surface during reduction to form inorganic interphases enriched in LiF and LiN_x, while the presence of organic IL cations facilitates the formation of organic species on the Li surface.[58] Others have shown that high inorganic-containing SEI may help stabilize the lithium-metal interface.[59,60]

The electrochemical stability window of the molten salt electrolytes was characterized using linear sweep voltammetry (LSV). The molten salts are stable up to ~5.3 V against SS (Figure 3A) and up to 6.0 V against aluminum at 80°C and 100°C (Figure 3B). In contrast, the IL electrolyte appears more vulnerable with SS (~4 V), yielding higher parasitic current densities, and does not appear to passivate aluminum. Potentiostatic hold measurements (Figures 3C and S6), where the aluminum working electrode is held at increasingly higher potentials, corroborate the LSV measurements with oxidative stability of $Li_{0.30}K_{0.35}Cs_{0.35}FSA > Li_{0.45}K_{0.55}FSA >> Pyr_{14}FSA$. Hence, high-voltage electrodes can be readily supported. Anodic dissolution of the Al current collector and/or oxidative decomposition of electrolytes is often encountered at high voltages, especially with amide-based salts.[13] Remarkably, SEM in Figures 3D and S7 demonstrates no corrosion of the Al working electrode with the ternary $Li_{0.30}K_{0.35}Cs_{0.35}FSA$ mixture after holding a Li‖Al cell for 72 h at 5.5 V and 80°C. The SEM images align with the LSV data in Figure 3B, which shows the stability of the molten salt mixtures against Al. Using a reported mechanism,[61] we attribute the surprising stability to an inability of the AlF_3 corrosion product to dissolve in the molten salt. Instead, the aluminum remains passivated, and corrosion is effectively suppressed. A similar morphology is also observed for the binary $Li_{0.45}K_{0.55}FSA$ electrolyte (Figure S7). In contrast, holes and cracks in the Al surface are
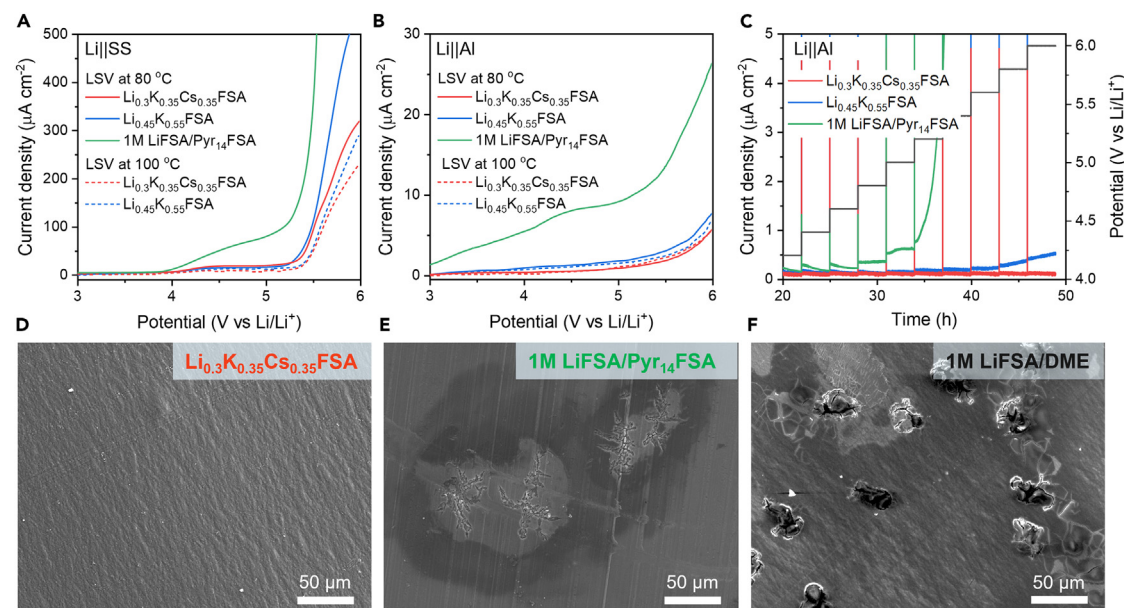
Figure 3. Oxidative stability
Linear sweep voltammetry (LSV) curves at 1 mV s^{-1} of the molten salt electrolytes and IL electrolyte.
(A) Li||SS cells at 80°C and 100°C.
(B) Li||Al cells at 80°C and 100°C.
(C) Potentiostatic hold of the molten salt electrolytes using Li||Al cells at 80°C. Cells were held at a specific voltage for 3 h between 3 and 6 V with an interval of 0.2 V.
(D) SEM images of Al surfaces in the Li||Al cells, which were held at 5.5 V for 72 h using $Li_{0.30}K_{0.35}Cs_{0.35}FSA$ electrolyte at 80°C.
(E) SEM images of Al surfaces in the Li||Al cells, which were held at 5.5 V for 72 h using 1 M LiFSA/Pyr$_{14}$FSA electrolyte at 80°C.
(F) SEM images of Al surfaces in the Li||Al cells, which were held at 5.5 V for 72 h using 1 M LiFSA/DME electrolytes at 20°C. SS, stainless steel spacer; Al, aluminum.

observed when 1 M LiFSA/Pyr$_{14}$FSA (Figure 3E) and 1 M LiFSA/DME (Figure 3F) electrolytes are used with the same electrochemical protocol.

Lithium-metal cycling

The CE of lithium plating and stripping from lithium-metal anodes (LMAs) using both the $Li_{0.45}K_{0.55}FSA$ (Figure S8) and $Li_{0.30}K_{0.35}Cs_{0.35}FSA$ (Figure S9) molten salt electrolytes as well as the 1 M LiFSA/Pyr$_{14}$FSA IL electrolytes (Figure S10) was investigated in Li||Cu cells at different current densities at 80°C and 100°C (Figure 4A). The ternary $Li_{0.30}K_{0.35}Cs_{0.35}FSA$ electrolyte exhibits higher CE compared to the binary $Li_{0.45}K_{0.55}FSA$ and 1 M LiFSA/Pyr$_{14}$FSA electrolytes, where higher temperatures and lower current densities yield higher CE. At 80°C and a current density of 0.5 mA cm^{-2}, the CE of the LMA using the binary $Li_{0.30}K_{0.35}Cs_{0.35}FSA$ electrolyte is roughly 99.15%, which is much higher than the cells cycled in the 1 M LiFSA/Pyr$_{14}$FSA electrolyte (96.65%) or 1 M LiFSA/DME (98.4%, cycled at 20°C).[12] The effects of current density on the CEs of LMAs were also studied at 100°C, where at a current of 1 mA cm^{-2}, CE improved from 90.76% to 98.34% in the binary molten salt electrolyte and from 98.11 to 99.44% in the ternary counterpart. Interestingly, both electrolytes demonstrated high CEs at a very high current densities of 3.0 mA cm^{-2} at 100°C: 92.88% and 96.58% for the binary and ternary electrolytes, respectively. We primarily attribute the improvement in CE at higher temperatures to the viscosity decrease and to the increase in ionic conductivity and LTN of the molten salts, which may facilitate the Li$^+$ stripping/plating process. The current density of 3.0 mA cm^{-2} is equivalent to 1C rate for cells with practical areal capacity loading of 3.0 mAh cm^{-2}, which meets the requirements for most industrial applications.[57]
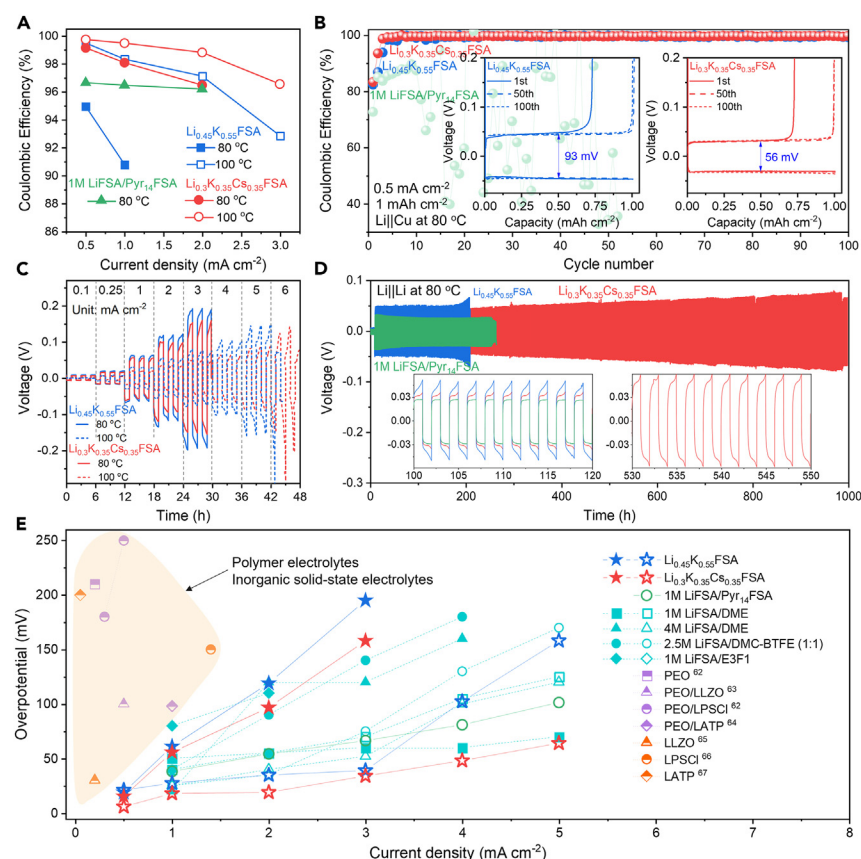
Figure 4. Lithium-metal cycling

(A) Li plating/stripping Coulombic efficiency cycled at various current densities and temperatures.

(B) Long-term cycling of Li||Cu cells cycled at 0.5 mA cm^{-2} to 1 mAh cm^{-2} at 80°C; the insets show the overpotential profiles at the selected cycles.

(C) Rate performance of the Li||Li cells cycled at different current densities increasing from 0.1 to 6 mA cm^{-2} at 80°C and 100°C.

(D) Long-term Li||Li cell cycling cycled at a current density of 1 mA cm^{-2} to 1 mAh cm^{-2} at 80°C.

(E) A summary of the overpotential of Li||Li cells using different types of electrolytes at various current densities at 20°C and elevated temperatures. For liquid electrolytes (cyan symbols), the solid and open symbols indicate that the cells were cycled at 20°C and 60°C, respectively. For the organic IL electrolyte (1 M LiFSA/Pyr$_{14}$FSA, green open symbol), the cells were cycled at 80°C. For molten salt electrolytes (star symbols), the solid and open symbols represent the cells cycled at 80°C and 100°C, respectively. For polymer composites (purple symbols) and inorganic electrolytes (orange symbols), the half-up solid symbols represent the cells cycled at elevated temperatures, respectively. The lines are to guide the eyes.

In addition to high CE, the long-term cycling stability of LMAs is also critical for rechargeable LMBs. The evolution of voltage profiles and CE of Li||Cu cells during Li plating/stripping was further examined at a current density of 0.5 mA cm^{-2} with a capacity of 1 mAh cm^{-2} (Figure 4B, inset). The molten salt electrolytes enable a lifetime of over 100 cycles, with an average CE of ≈99.5% and no obvious voltage polarization increase. However, the cells using the 1 M LiFSA/Pyr$_{14}$FSA electrolyte show a cycling ability of up to 20 cycles with an increase in CE from 70% to 90%, and a large fluctuation in CE can be observed for the later cycles (Figure S11). Electrode polarization during cycling in the ternary electrolyte (56 mV) is much lower than that in the binary electrolyte (93 mV) due to the reduced viscosity and improved ionic conductivity of the ternary electrolytes. Additionally, the Li||Cu cells show initial CEs of 83% and 84%, for the binary and ternary electrolytes, respectively, which are

higher than that of the 1 M LiFSA/Pyr$_{14}$FSA electrolyte (70%). The relatively low initial CE of the IL electrolyte may be due to the formation of unstable organic-based SEI layer.[62,63] After 10 cycles, the CE of the molten salt electrolytes increased to and stabilized at 99%, which suggests the formation of a stable SEI.

It is crucial to evaluate the interfacial stability of low-melting molten salt electrolytes and lithium-metal electrodes. First, the critical current density (CCD) for the molten salt electrolytes using symmetrical Li||Li cells was performed from 1 to 6 mA cm^{-2} at 80°C and 100°C. For each current density, the cells were subjected to three cycles (a total of 2 h per cycle). Figure 4C shows that the overpotentials of both binary and ternary electrolytes increased incrementally with current density, yet the overpotential of the ternary electrolytes is always lower than that of the binary electrolytes due to the lower viscosity and faster Li$^+$ transport. At 80°C, the ternary electrolytes show low overpotentials of 55 and 160 mV at 1 and 3 mA cm^{-2}, respectively. At 100°C, even lower overpotentials of only 10 mV at 1 mA cm^{-2} and 60 mV at a very high current density of 5 mA cm^{-2} suggest excellent reaction kinetics.

To analyze the stability and compatibility of molten salt electrolytes with lithium metal, the long-term cycling stability at a current density of 1 mA cm^{-2} with a capacity of 1 mAh cm^{-2} at 80°C is shown in Figure 4D. The cells using ternary electrolytes exhibit stable lithium plating and stripping over 1,000 h corresponding to 500 cycles, with an increase in overpotential from 30 to 65 mV. The voltage curves in the insets show smooth lithium plating and stripping with no sign of a soft short. Symmetric lithium cells with binary electrolytes were also cycled at 1 mA cm^{-2} at 80°C and 100°C, showing stable cycling up to 250 h at 80°C and 350 h at 100°C (Figure S12). The shortened cycle life of binary electrolytes at 80°C and higher overpotentials may be due to nonuniform Li deposits leading to the formation of dendrites in later cycles. In addition, a symmetric cell with the IL electrolyte (1 M LiFSA in Pyr$_{14}$FSA) was cycled at the same current density at 80°C. The cell exhibits lower overpotential (29 mV) compared to the cell with the ternary electrolytes, which is due to the higher ionic conductivity and lower viscosity of the IL electrolyte. However, the cell only shows stable cycling for 250 h, with a sudden drop in overpotential due to soft shorting. Similarly, the cells using the 1 M LiFSA/DME electrolyte also have a stable, low overpotential of roughly 30 mV over 240 h (Figure S13). Figure S14 presents the EIS spectra of both molten salt electrolyte cells before cycling and after 100 cycles, where a slight increase in interfacial resistance is observed for both electrolytes. These differences may be attributed to the formation and stabilization of the SEI layer for the molten salts.[18,64] In contrast, interfacial resistance increase appears higher for 1 M LiFSA in IL (Figure S14) and DME[12] electrolytes. Additionally, Figure S12 shows the galvanostatic cycling of symmetric lithium cells with the ternary Li$_{0.30}$K$_{0.35}$Cs$_{0.35}$FSA electrolyte at 2 and 4 mA cm^{-2} with a capacity of 1 mAh cm^{-2} per half cycle and stable lithium plating and stripping up to 350 cycles and 200 cycles, respectively, and only a slight increase in the overpotential is observed.

Figure 4E compares the overpotential of molten salt electrolytes with literature-reported small-molecule liquid electrolytes, IL electrolytes, polymers/polymer-composite-based solid-state electrolytes,[65–67] and inorganic solid-state electrolytes[68–70] at various current densities and temperatures. At elevated temperatures, there is a negligible difference in the overpotentials between our molten salt electrolytes (100°C) and state-of-the-art liquid (at room temperature) or IL electrolytes (cycled at 60°C). For instance, the overpotential of Li$_{0.30}$K$_{0.35}$Cs$_{0.35}$FSA electrolyte cells measured at 80°C is roughly 96 mV at 2 mA cm^{-2}, while that of 4 M LiFSA/DME

and 2.5 M LiFSA/DMC-BTFE (dimethyl carbonate-bis(2,2,2-trifluoroethyl) ether; 1:1, v/v) measured at 20°C are around 100 and 90 mV, respectively. The low overpotential indicates low resistance at the interfaces between electrolytes and electrodes due to a uniform SEI layer that enhances long-term cycling[71] without the safety hazards of liquids. Remarkably, the overpotentials of molten salt electrolytes (15–20 mV) are distinctly lower than those of polymers, polymer-inorganic composites, and inorganic-based solid-state electrolytes (50–100 mV) at 0.5 mA cm^{-2} at 60°C, with much higher current densities accessible in the molten salts.

To elucidate the compatibility of the low-melting molten salt electrolytes with a Ni-rich cathode, Li∥NMC811 coin cells using binary $Li_{0.45}K_{0.55}FSA$, ternary $Li_{0.30}K_{0.35}Cs_{0.35}FSA$, and 1 M LiFSA/$Pyr_{14}$FSA electrolytes employing thick Li anodes (500 μm) were assembled and cycled in the voltage window of 3–4.3 V at a temperature of 80°C. For room temperature comparison, a conventional state-of-the-art liquid electrolyte (1 M LiFSA/DME) was used. After five formation cycles at C/20, the cells were cycled with an increment discharge rate up to 1C (1C = 1.66 mA cm^{-2}) (Figure S14). Strikingly, the capacity delivered in the ternary $Li_{0.30}K_{0.35}Cs_{0.35}FSA$ electrolyte is close to that of the IL electrolyte up to the rate of C/3 and is markedly higher than that of the 1 M LiFSA/DME electrolyte, which performs similarly to the binary $Li_{0.45}K_{0.55}FSA$ electrolyte. The cyclability of the Li∥NMC811 cells using different electrolytes was further evaluated at C/3 charge after three formation cycles at C/20 (Figures 5A, 5B, and S15). Cells using binary and ternary molten salts as electrolytes show the same trend of a gradual decrease in capacity up to 200 cycles, while the IL electrolyte (1 M LiFSA/Pyr_{14}FSA) and liquid electrolyte (1 M LiFSA/DME) show a sharp fade in discharge capacity after 80 and 50 cycles, respectively. For example, the cell with 1 M LiFSA/DME as its electrolyte loses 20% of its discharge capacity after only 50 cycles due to the poor electrolyte stability at both the Li anode and the high-voltage NMC811 cathode.[12] Meanwhile, the discharge capacity of the IL electrolyte (1 M LiFSA/Pyr_{14}FSA) cells shows a capacity retention of only 39% at the 200th cycle. Strikingly, both ternary and binary electrolytes maintain superior discharge capacities of 178 and 154 mAh g^{-1} at the 100th cycle, respectively, and then reach a capacity retention of 75% and 67% at the 200th cycle. Table S3 shows that the performance of the molten salt electrolytes in the Li∥NMC811 full cells is one of the best in comparison to state-of-the-art liquid electrolytes. This remarkable cycling stability demonstrates the excellent compatibility of both electrolytes with the Ni-rich NMC811 and the stable SEI layer formed on the LMA. As shown in Figure 5A, the initial CEs of the cells employing $Li_{0.45}K_{0.55}FSA$ and $Li_{0.30}K_{0.35}Cs_{0.35}FSA$ are 89.4% and 92.1%, respectively, which are higher than that of the 1 M LiFSA/Pyr_{14}FSA (89.2%) and 1 M LiFSA/DME (86.7%) electrolytes. This indicates that more side reactions occur during the initial charge of NMC811 in the IL electrolyte and organic liquid electrolytes than in the molten salt electrolytes. From the 10th to 200th cycles, the CE of the molten salt electrolytes is higher than 99.5%, while that of the IL electrolyte is around 98.7%, and the CE of 1 M LiFSA/DME electrolytes is unstable.

In an effort to benchmark practical cell conditions, cells with NMC811 cathodes (9 mg cm^{-2}) and thin LMAs (20 μm) (negative/positive ratio of 2.2) were assembled (Figures 5C and S16). The voltage profiles of the cells employing molten salts as electrolytes at a few selected cycles are shown in Figures 5D and S15. For the thin Li∥NMC811 cells, the reduced areal capacity of LMBs using molten salt electrolytes does not severely accelerate the capacity fade up to 100 cycles. A discharge capacity of ∼170 mAh g^{-1} at the 100th cycle can be observed for both molten salt electrolytes, corresponding to a capacity retention of 81%. Nevertheless, the performance of the molten salt electrolytes in the Li∥NMC811 cells is superior to the IL electrolyte
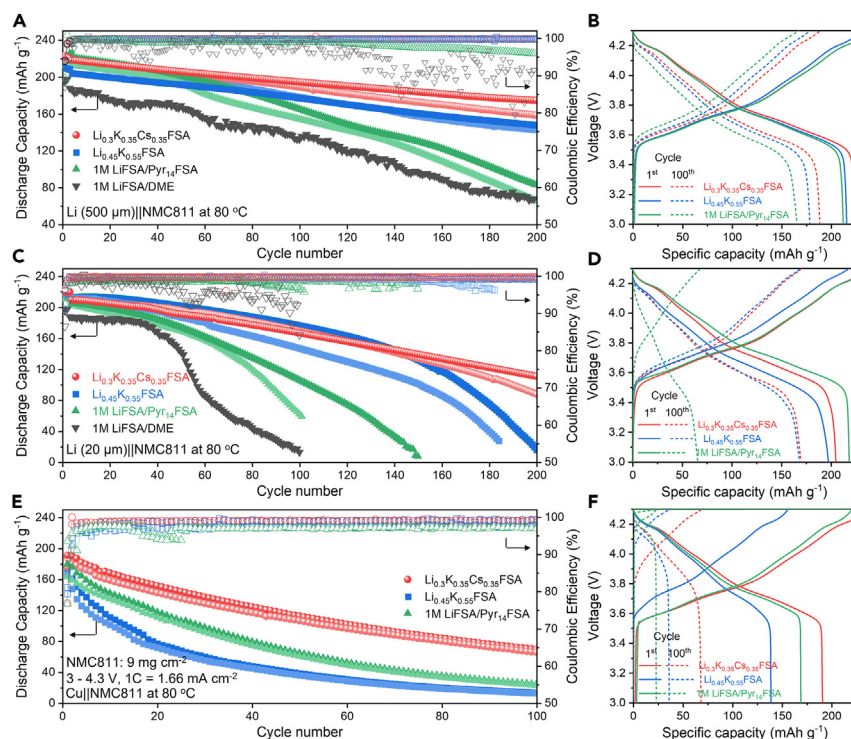
Figure 5. Battery cycling performance and selected voltage profiles

(A and B) Li (500 μm)||NMC811 cells at a constant discharge and charge rate of C/3 for molten salt electrolytes, 1 M LiFSA/Pyr$_{14}$FSA, and 1 M LiFSA/DME electrolytes.

(C and D) Thin Li (20 μm)||NMC811 cells at a constant discharge and charge rate of C/3 for molten salt electrolytes, 1 M LiFSA/Pyr$_{14}$FSA, and 1 M LiFSA/DME electrolytes.

(E and F) Cu||NMC811 cells at a constant discharge and charge rate of C/3 for molten salt electrolytes, 1 M LiFSA/Pyr$_{14}$FSA, and 1 M LiFSA/DME electrolytes.

Multiple coin cells are shown in (A), (C), and (E) to show reproducibility. Cells with molten salt electrolytes and IL electrolytes were cycled at 80°C, while 1 M LiFSA in DME was cycled at 20°C.

and conventional liquid electrolytes. The cells with the 1 M LiFSA/DME (Figure S16) and 1 M LiFSA/Pyr$_{14}$FSA electrolytes lasted for 40 and 60 cycles, respectively, followed by a drastic decay, mainly due to the decomposition of electrolytes and Li dendrite formation.[7,16] The remarkable cycle life of the molten salt electrolytes compared to the conventional liquid electrolytes may be a result of the higher compatibility of molten salts toward both LMAs and NMC811 cathodes and of the stable SEI formation.

Furthermore, "anode-free" Cu|NMC811 cells were fabricated and characterized, and the capacity and CE are shown in Figure 5E. The voltage profiles at the selected cycles are shown in Figure 5F. At the 100th cycle, the cell employing the ternary Li$_{0.30}$K$_{0.35}$Cs$_{0.35}$FSA electrolyte exhibits a capacity of 75 mAh g^{-1} corresponding to a capacity retention of 40%, while the cell employing the IL electrolyte quickly decays to the same capacity in only 30 cycles. Such improved cycle life is expected due to the higher CE of the lithium stripping/plating processes in the molten salt Li$_{0.30}$K$_{0.35}$Cs$_{0.35}$FSA electrolytes than in the IL electrolytes, which is a limiting factor for the cycling stability of the anode-free cells.[72] In addition, Table S4 shows that the performance of the anode-free cell using the ternary Li$_{0.30}$K$_{0.35}$Cs$_{0.35}$FSA molten salt electrolyte is comparable to state-of-the-art volatile liquid electrolytes.

Matter
Article

CellPress

Conclusions

In this study, we introduce solvent-free, low-melting, alkali-based molten salt electrolytes for high-energy-density LMBs. Alkali-based molten salts avoid the challenges of organic-cation-containing ILs, which are vulnerable to degradation, as well as the safety hazards of conventional liquid electrolytes. Furthermore, they avoid the poor electrode/electrolyte interfaces of safer polymer and inorganic solid-state conductors. Binary $Li_{0.45}K_{0.55}FSA$ and ternary $Li_{0.30}K_{0.35}Cs_{0.35}FSA$ mixtures exhibit T_ms at 68°C and 45°C, good ionic conductivities ~1 mS cm^{-1} at 60°C, high oxidative stabilities up to 6 V (vs. Li/Li$^+$), and aluminum passivation. These molten salt electrolytes can support lithium-metal CE as high as 99.8% and uniform nodule-like compact deposition morphologies. Furthermore, the metal interface is enriched with an inorganic-anion-derived SEI. These molten salts can support current densities as high as 5 mA cm^{-2} with low overpotential, leading to similarities to flammable, highly concentrated electrolytes while outperforming solid-state polymer and inorganic electrolytes. Finally, these molten salt electrolytes show superior compatibility to high-voltage cathode materials such as NMC811 at 80°C, delivering a specific capacity of >150 mAh g^{-1} and an average CE of >99.65% over 100 cycles, which outperforms IL electrolytes (1 M LiFSA/Pyr$_{14}$FSA) and conventional liquid electrolytes (1 M LiFSA/DME). Our work highlights the need for novel electrolyte classes to accelerate the development and deployment of energy-dense LMBs.

EXPERIMENTAL PROCEDURES

Resource availability

Lead contact

Further information and requests for resources should be directed to and will be fulfilled by the lead contact, Dr. Chibueze V. Amanchukwu (chibueze@uchicago.edu).

Materials availability

This study did not generate new unique reagents.

Data and code availability

All data reported in this study will be shared by the lead contact upon request. This paper does not report original code.

Electrolyte materials and preparation

LiFSA (purity ≥ 99%) salt was received from Arkema (Colombes, France). KFSA (purity ≥ 98%) was purchased from FUJIFILM Wako Pure Chemical Corporation (Tokyo, Japan), while CsFSA (purity ≥ 98%) salts were purchased from Provisco CS S.R.O. (Brno-Královo Pole, Czech Republic). All salts were dried at 100°C for 3 days under vacuum in an integrated heating antechamber and kept inside an argon-filled glovebox (VigorTech) with both O_2 and H_2O content less than 1 ppm. Pyr$_{14}$FSA (purity ≥ 98%) IL was purchased from IoLiTec (Heilbronn, Germany). It was stored in a vial containing 4 Å molecular sieves and kept inside an argon-filled glovebox. The water content of single salts was below 20 ppm based on Karl-Fischer titration measurements. All solvents—DME (1,2-dimethoxyethane), BTFE (bis(2,2,2-trifluoroethyl) ether), and DMC (dimethylcarbonate)—were purchased from Sigma Aldrich (Burlington, MA, USA) with high purity (99.5%) and dried using 4 Å molecular sieves. E3F1 was synthesized according to previously reported techniques.[53]

The binary and ternary alkali-metal molten salt electrolytes were prepared by mixing the salts at specific mole ratios and crushing them using a mortar and pestle at room

Matter
Article

temperature in an argon-filled glovebox (VigorTech). The 1 M LiFSA-based Pyr$_{14}$FSA IL electrolyte (1 M LiFSA/Pyr$_{14}$FSA) and liquid electrolytes of 1 M LiFSA/DME, 4M LiFSA/DME, 2.5 M LiFSA/DMC-BTFE (1:1, v/v), and 1 M LiFSA/E3F1 were prepared by stirring for 12 h. Electrolytes were kept in the Ar-filled glovebox with both O_2 and H_2O content being less than 1 ppm before use.

Coin cell assembly

All coin cell (CR2032) parts were ordered from Xiamen TOB New Energy Technology (Fujian, China). Lithium foil (thickness: 500 μm, purity: 99.9%, MTI) was brushed to remove oxide layers and cut into disks 12 mm in diameter. Celgard 3501 separators (3501, 25 μm thick) were cut into 18 mm disks and vacuum dried at 70°C. Whatman glass fiber separator (WM, GE Healthcare Life Science) was cut into 18 mm disks, rinsed with acetone 3 times, and then vacuum dried at 70°C for 1 day. The LiNi$_{0.8}$Co$_{0.1}$Mn$_{0.1}$O$_2$ (NMC811) electrode was received from the Cell Analysis, Modeling, and Prototyping (CAMP) facility at Argonne National Laboratory. The NMC811 electrode has a total mass loading of ~9 mg cm^{-2} with 90 wt % Targray NMC811, 5 wt % Timcal C45 carbon, and 5 wt % Solvay 5130 PVDF binder. The NMC811 electrode was cut into disks with a diameter of 12 mm and dried at 120°C overnight in a heated glovebox antechamber.

The cells for cycling were then assembled using the following procedure (Figure S17). First, working and counter electrodes were placed on a hot plate. 100 mg electrolytes were poured on each electrode and heated at 120°C until the electrolyte was fully melted. A spring was placed on the negative case, and one piece of stainless steel spacer (SS) was then placed on the spring. The counter electrode with the melted electrolytes was placed in the center of the SS. After that, a piece of separator (Celgard 3501, 18 mm in diameter) was placed on the melted electrolyte, and a light pressure was applied to guarantee that the separator was fully wet. Subsequently, the working electrode (cathode disk) with a melted electrolyte was placed on top of the separator. Finally, the Al disk (18 mm in diameter) and the Al-coated positive case (Al-Clad CR2032, MTI) were subsequently placed, and the cell was vacuumed in the glovebox antechamber for 2 min to remove any bubbles in the electrolyte and ensure the wetting of the separator prior to coin cell crimping at 700 MPa (TOB-DF-160, Xiamen TOB New Energy Technology).

Physical characterizations

Differential scanning calorimetry (DSC)

A differential scanning calorimeter (DSC 2500, TA Instruments) was utilized to measure the melting transition temperature of the electrolytes. An amount of electrolyte (~12 mg) was added and sealed in a Tzero pan with a hermetic lid inside an argon-filled glovebox (O_2, H_2O < 1 ppm). Samples were equilibrated at −80°C and looped between −80°C and 150°C three times with a ramping rate of 10°C min^{-1}. The coin cells for metal deposits were heated up at 120°C for 10 min and decrimped directly. The separator and metal deposited on copper were collected and washed with fresh DME solvent for 2 min 5 times to remove residual electrolytes. The DSC of the samples were measured in the temperature range of −80°C and 150°C with the heating rate of 10°C min^{-1}.

Scanning electron microscopy (SEM)

Field-emission SEM (Carl Zeiss Merlin) was utilized to observe the morphology of the electrodes with an accelerating voltage of 15 kV. The metal deposited on the copper electrodes was prepared at different capacities using a Biologic MPG-2 potentiostat. Afterward, cells were directly transferred and decrimped in an argon-filled glovebox

Matter
Article

(O_2, H_2O < 1 ppm). The copper electrodes with the deposited metal coating were immersed in the DME solvent to remove residual electrolytes and dried under vacuum in the small chamber of the glove box for 5 min before SEM observation.

Chemical characterization
X-ray photoelectron spectroscopy (XPS)
XPS was utilized to characterize the chemical compositions of the metal deposits on the copper electrode samples. In an argon glovebox, coin cells were first heated on the hot plate surface at 120°C for 15 min and decrimped. The electrodes were carefully collected and immersed in DME solvent for 2 min 5 times to remove residual electrolytes. The samples were then placed in glass vials and dried in the small antechamber of the glove boxes under low pressure (−0.1 MPa) for 10 min. XPS characterization was conducted using the PHI 5000 VersaProbe II System (Physical Electronics) with an Al Ka radiation ($h\nu$ = 1,486.6 eV) beam (100 μm, 25 W). There was less than 5 s air exposure during sample transfer to the instrument. Peaks were fitted using CasaXPS software.[73]

Inductively coupled plasma mass spectrometry (ICP-MS)
The ICP-MS technique was used to confirm the chemical compositions of electrolytes and metal deposits on copper. Coin cells were heated on the hot plate surface at 120°C for 15 min and decrimped. The electrodes and separators were collected and performed the ICP-MS without washing so there was no chance that K and Cs metals (if they are deposited) could be eliminated. Samples were then moved outside the glove box and dissolved in 5 mL deionized water (18.2 MΩ cm^{-1}) for 1 h. A (3% v/v) HNO_3 solution (TraceMetal Grade, Thermo Fisher Scientific) was prepared and used as a matrix for further dilutions. All measurements used either Thermo iCAP Q ICP-MS or Thermo iCAP RQ ICP-MS.

Electrochemical characterization
Electrochemical impedance spectroscopy (EIS)
Coin cells used for EIS measurement were assembled using SS as the counter and working electrodes. Coin cells were heated inside an ESPEC environmental chamber (BTZ-133). The temperature was first set and held at 120°C for 20 h and then cooled to 20°C with an interval of 10° while holding at each temperature for 1 h. Afterward, impedance spectroscopy was performed (7 MHz–100 Hz, 10 mV amplitude) using a Biologic VSP-300 Potentiostat. The ionic conductivity (σ) was calculated by the following equation: σ = L/(R × S), where L represents the thickness of the Whatman separator, R is the impedance at different temperatures, and S is the contact area between the electrolyte and blocking electrodes. For cells with a Whatman separator, a cell constant of 31.1 was used. The cell constant was calculated using the ternary $Li_{0.30}K_{0.35}Cs_{0.35}FSA$ molten salt conductivity measured using a PTFE ring shim (thickness of 0.005 in, inner diameter of 0.25 in) as a spacer between two SS electrodes (no separator).

Linear sweep voltammetry (LSV) and potentiostatic hold
LSV and potentiostatic hold were performed using a Biologic MPG-2 potentiostat using two different working electrodes of SS and Al foil (20 μm, Thermo Fisher Scientific). The cells were rested for 20 h at a specific temperature in an ESPEC environmental chamber (BTZ-133). In the LSV test, the cell voltage was scanned from the open-circuit voltage to 6 V at a rate of 1 mV s^{-1}. In the potentiostatic hold test, the cell voltage was held for 3 h at each voltage from 3 to 6 V with an interval of 0.2 V. The cells were held at the tested temperatures using an ESPEC environmental chamber (BTZ-133).

Symmetric Li//Li cell cycling

A Neware BTS4000 battery tester was utilized to cycle Li||Li coin cells at temperatures of 80°C and 100°C in the heating chambers of a Memmert IN 110 oven and a Binder ED056UL (FLW), respectively. For the CCD test, the cells were rested for 20 h at specific temperatures and had five formation cycles at 0.1 mA cm^{-2} to 0.1 mAh cm^{-2}. Subsequently, the Li||Li cells were cycled at different current densities from 1 (capacity of 1 mAh cm^{-2}) to 6 mA cm^{-2} (capacity of 6 mAh cm^{-2}). For long-term Li||Li cell cycling, the cells were rested for 20 h at specific temperatures and had five formation cycles at 0.1 mA cm^{-2} to 0.1 mAh cm^{-2} and then were cycled at different current densities and capacities, respectively. The cycling was performed with cutoff voltages that were set to be −2 and 1 V for discharge and charge, respectively.

Coulombic efficiency (CE) measurement in Li//Cu cells

The CE measurement was applied using a previously published protocol.[11] First, Li was deposited on the Cu electrode at a current density of 0.5 mA cm^{-2} to 5 mAh cm^{-2} and stripped to 1 V. Another 10 h of Li deposition at a current density of 0.5 mA cm^{-2} was continued. Afterward, Li was stripped and plated on Cu electrodes for 10 cycles at a current density of 0.5 mA cm^{-2} to 1 mAh cm^{-2}. Finally, lithium was stripped from the Cu electrode until the cell voltage reached 1 V. CE was calculated as the ratio of total stripping capacity over total plating capacity (except for the precycle). The long-term cycling of Li||Cu cells was also performed, in which Li was deposited on Cu for 2 h and stripped until the voltage reached 1 V. The applied current density was 0.5 mA cm^{-2}. The CE measurements were performed at temperatures of 80°C and 100°C in the heating chambers of a Memmert IN 110 oven and a Binder ED056UL (FLW), respectively.

Full cell cycling

The charge/discharge rate was calculated based on the exact mass of cathode material in which NMC811 has a full capacity of 203 mAh g^{-1}. The mass loading of cathode NMC811 material is around 9 mg cm^{-2}, which is equivalent to 1C ≈ 1.66 mA cm^{-2}. An aluminum-coated coin cell case was used. A Celgard 3501 separator was used. A Neware BTS4000 battery tester was used to cycle coin cells at temperatures of 80°C and 100°C in the heating chambers of Memmert IN 110 and a Binder ED056UL (FLW), respectively. The cells had 3 formation cycles at the C/20 rate and were later cycled at specific C rates at specific temperatures. The total mass of the Li|| NMC811 coin cell (including every part) was 3.644 g.

SUPPLEMENTAL INFORMATION

Supplemental information can be found online at https://doi.org/10.1016/j.matt.2023.10.017.

Matter
Article

CellPress

AUTHOR CONTRIBUTIONS

M.C.V. and C.V.A. designed the experiments. M.C.V. and H.S.S. conducted thermal analysis and measured ionic conductivities. M.C.V. conducted electrochemical measurements with the assistance of P. Mirmira, P. Ma, and E.S.D. R.J.G. performed ICP-MS measurements. C.V.A. conceived and supervised the project. M.C.V. and C.V.A. wrote the manuscript. All authors discussed the results and reviewed the manuscript.

DECLARATION OF INTERESTS

REFERENCES

1. Dunn, B., Kamath, H., and Tarascon, J.M. (2011). Electrical energy storage for the grid: A battery of choices. Science *334*, 928–935. https://doi.org/10.1126/science.1212741.

2. Choi, J.W., and Aurbach, D. (2016). Promise and reality of post-lithium-ion batteries with high energy densities. Nat. Rev. Mater. *1*, 16013–16016. https://doi.org/10.1038/natrevmats.2016.13.

3. Duffner, F., Kronemeyer, N., Tübke, J., Leker, J., Winter, M., and Schmuch, R. (2021). Post-lithium-ion battery cell production and its compatibility with lithium-ion cell production infrastructure. Nat. Energy *6*, 123–134. https://doi.org/10.1038/s41560-020-00748-8.

4. Cao, Y., Li, M., Lu, J., Liu, J., and Amine, K. (2019). Bridging the academic and industrial metrics for next-generation practical batteries. Nat. Nanotechnol. *14*, 200–207. https://doi.org/10.1038/s41565-019-0371-8.

5. Liu, B., Zhang, J.-G., and Xu, W. (2018). Advancing Lithium Metal Batteries. Joule *2*, 833–845. https://doi.org/10.1016/j.joule.2018.03.008.

6. Liu, J., Bao, Z., Cui, Y., Dufek, E.J., Goodenough, J.B., Khalifah, P., Li, Q., Liaw, B.Y., Liu, P., Manthiram, A., et al. (2019). Pathways for practical high-energy long-cycling lithium metal batteries. Nat. Energy *4*, 180–186. https://doi.org/10.1038/s41560-019-0338-x.

7. Qian, J., Henderson, W.A., Xu, W., Bhattacharya, P., Engelhard, M., Borodin, O., and Zhang, J.G. (2015). High rate and stable cycling of lithium metal anode. Nat. Commun. *6*, 6362. https://doi.org/10.1038/ncomms7362.

8. Lin, D., Liu, Y., and Cui, Y. (2017). Reviving the lithium metal anode for high-energy batteries. Nat. Nanotechnol. *12*, 194–206. https://doi.org/10.1038/nnano.2017.16.

9. Tikekar, M.D., Choudhury, S., Tu, Z., and Archer, L.A. (2016). Design principles for electrolytes and interfaces for stable lithium-metal batteries. Nat. Energy *1*, 16114. https://doi.org/10.1038/nenergy.2016.114.

10. He, X., Bresser, D., Passerini, S., Baakes, F., Krewer, U., Lopez, J., Mallia, C.T., Shao-Horn, Y., Cekic-Laskovic, I., Wiemers-Meyer, S., et al. (2021). The passivity of lithium electrodes in liquid electrolytes for secondary batteries. Nat. Rev. Mater. *6*, 1036–1052. https://doi.org/10.1038/s41578-021-00345-5.

11. Adams, B.D., Zheng, J., Ren, X., Xu, W., Zhang, J.-G., Adams, B.D., Zhang, J.-G., Zheng, J., Ren, X., and Xu, W. (2018). Accurate Determination of Coulombic Efficiency for Lithium Metal Anodes and Lithium Metal Batteries. Adv. Energy Mater. *8*, 1702097. https://doi.org/10.1002/aenm.201702097.

12. Yu, Z., Wang, H., Kong, X., Huang, W., Tsao, Y., Mackanic, D.G., Wang, K., Wang, X., Huang, W., Choudhury, S., et al. (2020). Molecular design for electrolyte solvents enabling energy-dense and long-cycling lithium metal batteries. Nat. Energy *5*, 526–533. https://doi.org/10.1038/s41560-020-0634-5.

13. Qiao, L., Oteo, U., Martinez-Ibañez, M., Santiago, A., Cid, R., Sanchez-Diez, E., Lobato, E., Meabe, L., Armand, M., and Zhang, H. (2022). Stable non-corrosive sulfonimide salt for 4-V-class lithium metal batteries. Nat. Mater. *21*, 455–462. https://doi.org/10.1038/S41563-021-01190-1.

14. Ren, X., Chen, S., Lee, H., Mei, D., Engelhard, M.H., Burton, S.D., Zhao, W., Zheng, J., Li, Q., Ding, M.S., et al. (2018). Localized high-concentration sulfone electrolytes for high-efficiency lithium-metal batteries. Chem *4*, 1877–1892. https://doi.org/10.1016/j.chempr.2018.05.002.

15. Chen, S., Zheng, J., Mei, D., Han, K.S., Engelhard, M.H., Zhao, W., Xu, W., Liu, J., and Zhang, J.G. (2018). High-voltage lithium-metal batteries enabled by localized high-concentration electrolytes. Adv. Mater. *30*, 1706102. https://doi.org/10.1002/adma.201706102.

16. Zhao, Y., Zhou, T., Ashirov, T., Kazzi, M.E., Cancellieri, C., Jeurgens, L.P.H., Choi, J.W., and Coskun, A. (2022). Fluorinated ether electrolyte with controlled solvation structure for high voltage lithium metal batteries. Nat.

Commun. *13*, 2575–2579. https://doi.org/10.1038/s41467-022-29199-3.

17. Zhao, Y., Zhou, T., Mensi, M., Choi, J.W., and Coskun, A. (2023). Electrolyte engineering via ether solvent fluorination for developing stable non-aqueous lithium metal batteries. Nat. Commun. *14*, 299. https://doi.org/10.1038/S41467-023-35934-1.

18. Wang, Z., Qi, F., Yin, L., Shi, Y., Sun, C., An, B., Cheng, H., and Li, F. (2020). An anion-tuned solid electrolyte interphase with fast ion transfer kinetics for stable lithium anodes. Adv. Energy Mater. *10*, 1903843. https://doi.org/10.1002/aenm.201903843.

19. Schkeryantz, L., Nguyen, P., McCulloch, W.D., Moore, C.E., Lau, K.C., and Wu, Y. (2022). K+ Single Cation Ionic Liquids Electrolytes with Low Melting Asymmetric Salt. J. Phys. Chem. C *126*, 11407–11413. https://doi.org/10.1021/acs.jpcc.2c03030.

20. Ding, F., Xu, W., Chen, X., Zhang, J., Engelhard, M.H., Zhang, Y., Johnson, B.R., Crum, J.V., Blake, T.A., Liu, X., and Zhang, J.G. (2013). Effects of Carbonate Solvents and Lithium Salts on Morphology and Coulombic Efficiency of Lithium Electrode. J. Electrochem. Soc. *160*, A1894–A1901. https://doi.org/10.1149/2.100310jes.

21. Jiao, S., Ren, X., Cao, R., Engelhard, M.H., Liu, Y., Hu, D., Mei, D., Zheng, J., Zhao, W., Li, Q., et al. (2018). Stable cycling of high-voltage lithium metal batteries in ether electrolytes. Nat. Energy *3*, 739–746. https://doi.org/10.1038/s41560-018-0199-8.

22. Yu, Z., Rudnicki, P.E., Zhang, Z., Huang, Z., Celik, H., Oyakhire, S.T., Chen, Y., Kong, X., Kim, S.C., Xiao, X., et al. (2022). Rational solvent molecule tuning for high-performance lithium metal battery electrolytes. Nat. Energy *7*, 94–106. https://doi.org/10.1038/s41560-021-00962-y.

23. Rustomji, C.S., Yang, Y., Kim, T.K., Mac, J., Kim, Y.J., Caldwell, E., Chung, H., and Meng, Y.S. (2017). Liquefied gas electrolytes for electrochemical energy storage devices. Science *356*, eaal4263. https://doi.org/10.1126/science.aal4263.

24. Yu, Z., Mackanic, D.G., Michaels, W., Lee, M., Pei, A., Feng, D., Zhang, Q., Tsao, Y., Amanchukwu, C.V., Yan, X., et al. (2019). A Dynamic, Electrolyte-Blocking, and Single-Ion-Conductive Network for Stable Lithium-Metal Anodes. Joule 3, 2761–2776. https://doi.org/10.1016/j.joule.2019.07.025.

25. Yamada, Y., Wang, J., Ko, S., Watanabe, E., and Yamada, A. (2019). Advances and issues in developing salt-concentrated battery electrolytes. Nat. Energy 4, 269–280. https://doi.org/10.1038/s41560-019-0336-z.

26. Garcia, B., Lavallée, S., Perron, G., Michot, C., and Armand, M. (2004). Room temperature molten salts as lithium battery electrolyte. Electrochim. Acta 49, 4583–4588. https://doi.org/10.1016/j.electacta.2004.04.041.

27. Niu, H., Wang, L., Guan, P., Zhang, N., Yan, C., Ding, M., Guo, X., Huang, T., and Hu, X. (2021). Recent Advances in Application of Ionic Liquids in Electrolyte of Lithium Ion Batteries. J. Energy Storage 40, 102659. https://doi.org/10.1016/j.est.2021.102659.

28. Macfarlane, D.R., Tachikawa, N., Forsyth, M., Pringle, J.M., Howlett, P.C., Elliott, G.D., Davis, J.H., Watanabe, M., Simon, P., and Angell, C.A. (2014). Energy applications of ionic liquids. Energy Environ. Sci. 7, 232–250. https://doi.org/10.1039/C3EE42099J.

29. Yang, Q., Zhang, Z., Sun, X.G., Hu, Y.S., Xing, H., and Dai, S. (2018). Ionic liquids and derived materials for lithium and sodium batteries. Chem. Soc. Rev. 47, 2020–2064. https://doi.org/10.1039/C7CS00464H.

30. Giffin, G.A. (2016). Ionic liquid-based electrolytes for "beyond lithium" battery technologies. J. Mater. Chem. A Mater. 4, 13378–13389. https://doi.org/10.1039/C6TA05260F.

31. Garcia, B., and Armand, M. (2004). Aluminium corrosion in room temperature molten salt. J. Power Sources 132, 206–208. https://doi.org/10.1016/j.jpowsour.2003.12.046.

32. Armand, M., Endres, F., MacFarlane, D.R., Ohno, H., and Scrosati, B. (2009). Ionic-liquid materials for the electrochemical challenges of the future. Nat. Mater. 8, 621–629. https://doi.org/10.1038/nmat2448.

33. Wang, D., Yang, J., He, P., and Zhou, H. (2021). A low-charge-overpotential lithium-CO 2 cell based on a binary molten salt electrolyte. Energy Environ. Sci. 14, 4107–4114. https://doi.org/10.1039/D1EE00068C.

34. Giordani, V., Tozier, D., Tan, H., Burke, C.M., Gallant, B.M., Uddin, J., Greer, J.R., McCloskey, B.D., Chase, G.V., and Addison, D. (2016). A Molten Salt Lithium-Oxygen Battery. J. Am. Chem. Soc. 138, 2656–2663. https://doi.org/10.1021/jacs.5b11744.

35. Xia, C., Kwok, C.Y., and Nazar, L.F. (2018). A high-energy-density lithium-oxygen battery based on a reversible four-electron conversion to lithium oxide. Science 361, 777–781. https://doi.org/10.1126/science.aas9343.

36. Liu, Q., Zhou, D., Shanmukaraj, D., Li, P., Kang, F., Li, B., Armand, M., and Wang, G. (2020). Self-Healing Janus Interfaces for High-Performance LAGP-Based Lithium Metal Batteries. ACS Energy Lett. 5, 1456–1464.

https://doi.org/10.1021/acsenergylett.0c00542.

37. Kohlmeyer, R.R., Horrocks, G.A., Blake, A.J., Yu, Z., Maruyama, B., Huang, H., and Durstock, M.F. (2019). Pushing the thermal limits of Li-ion batteries. Nano Energy 64, 103927. https://doi.org/10.1016/j.nanoen.2019.103927.

38. Kubota, K., Nohira, T., and Hagiwara, R. (2012). New inorganic ionic liquids possessing low melting temperatures and wide electrochemical windows: Ternary mixtures of alkali bis(fluorosulfonyl)amides. Electrochim. Acta 66, 320–324. https://doi.org/10.1016/j.electacta.2012.01.097.

39. Kubota, K., Nohira, T., and Hagiwara, R. (2010). Thermal properties of alkali bis(fluorosulfonyl) amides and their binary mixtures. J. Chem. Eng. Data 55, 3142–3146. https://doi.org/10.1021/je9010932.

40. Hagiwara, R., Tamaki, K., Kubota, K., Goto, T., and Nohira, T. (2008). Thermal properties of mixed alkali bis(trifluoromethylsulfonyl)amides. J. Chem. Eng. Data 53, 355–358. https://doi.org/10.1021/je700368r.

41. Tsuzuki, S., Kubota, K., and Matsumoto, H. (2013). Cation and anion dependence of stable geometries and stabilization energies of alkali metal cation complexes with FSA-FTA-and TFSA- anions: Relationship with physicochemical properties of molten salts. J. Phys. Chem. B 117, 16212–16218. https://doi.org/10.1021/jp409113z.

42. Kubota, K., and Matsumoto, H. (2014). Cation Mixtures of Alkali Metal (Fluorosulfonyl)(trifluoromethylsulfonyl)Amide as Electrolytes for Lithium Secondary Battery. J. Electrochem. Soc. 161, A902–A907. https://doi.org/10.1149/2.026406jes.

43. Phan, A.L., Jayawardana, C., Le, P.M., Zhang, J., Nan, B., Zhang, W., Lucht, B.L., Hou, S., Wang, C., Phan, A.L., et al. (2023). Solvent-Free Electrolyte for High-Temperature Rechargeable Lithium Metal Batteries. Adv. Funct. Mater. 33, 2301177. https://doi.org/10.1002/adfm.202301177.

44. Kubota, K., Tamaki, K., Nohira, T., Goto, T., and Hagiwara, R. (2010). Electrochemical properties of alkali bis(trifluoromethylsulfonyl)amides and their eutectic mixtures. Electrochim. Acta 55, 1113–1119. https://doi.org/10.1016/j.electacta.2009.09.024.

45. Yu, J., Zhai, W., Zhang, C., Wu, C., Wei, R., Chen, S., He, Y., Hu, Q., Yu, Y., and Liu, W. (2023). Solvent-Free and Long-Cycling Garnet-Based Lithium-Metal Batteries. ACS Energy Lett. 8, 1468–1476. https://doi.org/10.1021/acsenergylett.3c00088.

46. Rogers, D.J., and Janz, G.J. (1982). Melting-Crystallization and Premelting Properties of NaNO3-KNO3. Enthalpies and Heat Capacities. J. Chem. Eng. Data 27, 424–428. https://doi.org/10.1021/je00030a017.

47. Orozco, M.A., Acurio, K., Vásquez-Aza, F., Martínez-Gómez, J., and Chico-Proano, A. (2021). Thermal Storage of Nitrate Salts as Phase Change Materials (PCMs). Materials 14, 7223. https://doi.org/10.3390/ma14237223.

48. Domańska, U. (2010). Physico-Chemical Properties and Phase Behaviour of Pyrrolidinium-Based Ionic Liquids. Int. J. Mol.

Sci. 11, 1825–1841. https://doi.org/10.3390/ijms11041825.

49. Evans, J., Vincent, C.A., and Bruce, P.G. (1987). Electrochemical measurement of transference numbers in polymer electrolytes. Polymer 28, 2324–2328. https://doi.org/10.1016/0032-3861(87)90394-6.

50. Liu, X., Zarrabeitia, M., Mariani, A., Gao, X., Schütz, H.M., Fang, S., Bizien, T., Elia, G.A., Passerini, S., Liu, X., et al. (2021). Enhanced Li+ Transport in Ionic Liquid-Based Electrolytes Aided by Fluorinated Ethers for Highly Efficient Lithium Metal Batteries with Improved Rate Capability. Small Methods 5, 2100168. https://doi.org/10.1002/smtd.202100168.

51. Zhao, Y., Wang, L., Zhou, Y., Liang, Z., Tavajohi, N., Li, B., Li, T., Zhao, Y., Zhou, Y., Li, B., et al. (2021). Solid Polymer Electrolytes with High Conductivity and Transference Number of Li Ions for Li-Based Rechargeable Batteries. Adv. Sci. 8, 2003675. https://doi.org/10.1002/advs.202003675.

52. Amanchukwu, C.V., Yu, Z., Kong, X., Qin, J., Cui, Y., and Bao, Z. (2020). A New Class of Ionically Conducting Fluorinated Ether Electrolytes with High Electrochemical Stability. J. Am. Chem. Soc. 142, 7393–7403. https://doi.org/10.1021/jacs.9b11056.

53. Ma, P., Mirmira, P., and Amanchukwu, C.V. (2021). Effect of Building Block Connectivity and Ion Solvation on Electrochemical Stability and Ionic Conductivity in Novel Fluoroether Electrolytes. ACS Cent. Sci. 7, 1232–1244. https://doi.org/10.1021/acscentsci.1c00503.

54. Bale, C.W. (1989). The K-Li (Potassium-Lithium) system. Bulletin of Alloy Phase Diagrams 10, 262–264. https://doi.org/10.1007/BF02877508.

55. Ding, F., Xu, W., Graff, G.L., Zhang, J., Sushko, M.L., Chen, X., Shao, Y., Engelhard, M.H., Nie, Z., Xiao, J., et al. (2013). Dendrite-Free Lithium Deposition via Self-Healing Electrostatic Shield Mechanism. J. Am. Chem. Soc. 135, 4450–4456. https://doi.org/10.1021/ja312241y.

56. May, R., Zhang, Y., Denny, S.R., Viswanathan, V., and Marbella, L.E. (2020). Leveraging Cation Identity to Engineer Solid Electrolyte Interphases for Rechargeable Lithium Metal Anodes. Cell Rep. Phys. Sci. 1, 100239. https://doi.org/10.1016/j.xcrp.2020.100239.

57. Chen, S., Zheng, J., Yu, L., Ren, X., Engelhard, M.H., Niu, C., Lee, H., Xu, W., Xiao, J., Liu, J., and Zhang, J.G. (2018). High-Efficiency Lithium Metal Batteries with Fire-Retardant Electrolytes. Joule 2, 1548–1558. https://doi.org/10.1016/j.joule.2018.05.002.

58. Ren, X., Zou, L., Cao, X., Engelhard, M.H., Liu, W., Burton, S.D., Lee, H., Niu, C., Matthews, B.E., Zhu, Z., et al. (2019). Enabling high-voltage lithium-metal batteries under practical conditions. Joule 3, 1662–1676. https://doi.org/10.1016/j.joule.2019.05.006.

59. Xue, W., Shi, Z., Huang, M., Feng, S., Wang, C., Wang, F., Lopez, J., Qiao, B., Xu, G., Zhang, W., et al. (2020). FSI-inspired solvent and "full fluorosulfonyl" electrolyte for 4 V class lithium-metal batteries. Energy Environ. Sci. 13, 212–220. https://doi.org/10.1039/C9EE02538C.

60. von Aspern, N., Röschenthaler, G.V., Winter, M., and Cekic-Laskovic, I. (2019). Fluorine and

Matter
Article

lithium: ideal partners for high-performance rechargeable battery electrolytes. Angew. Chem. Int. Ed. *58*, 15978–16000. https://doi.org/10.1002/anie.201901381.

61. Yamada, Y., Chiang, C.H., Sodeyama, K., Wang, J., Tateyama, Y., and Yamada, A. (2015). Corrosion Prevention Mechanism of Aluminum Metal in Superconcentrated Electrolytes. Chemelectrochem *2*, 1687–1694. https://doi.org/10.1002/celc.201500235.

62. Xu, Y., Ding, T., Sun, D., Ji, X., Zhou, X., Xu, Y., Ding, T., Sun, D., Zhou, X., and Ji, X. (2023). Recent Advances in Electrolytes for Potassium-Ion Batteries. Adv. Funct. Mater. *33*, 2211290. https://doi.org/10.1002/adfm.202211290.

63. Adenusi, H., Chass, G.A., Passerini, S., Tian, K.V., Chen, G., Adenusi, H., Chen, G., Chass, G.A., Tian, K.V., and Passerini, S. (2023). Lithium Batteries and the Solid Electrolyte Interphase (SEI)-Progress and Outlook. Adv. Energy Mater. *13*, 2203307. https://doi.org/10.1002/aenm.202203307.

64. Mao, M., Ji, X., Wang, Q., Lin, Z., Li, M., Liu, T., Wang, C., Hu, Y.-S., Li, H., Huang, X., et al. (2023). Anion-enrichment interface enables high-voltage anode-free lithium metal batteries. Nat. Commun. *14*, 1082. https://doi.org/10.1038/s41467-023-36853-x.

65. Su, Y., Zhang, X., Du, C., Luo, Y., Chen, J., Yan, J., Zhu, D., Geng, L., Liu, S., Zhao, J., et al.

(2022). An All-Solid-State Battery Based on Sulfide and PEO Composite Electrolyte. Small *18*, 2202069. https://doi.org/10.1002/smll.202202069.

66. Wan, Z., Lei, D., Yang, W., Liu, C., Shi, K., Hao, X., Shen, L., Lv, W., Li, B., Yang, Q.H., et al. (2019). Low Resistance–Integrated All-Solid-State Battery Achieved by Li7La3Zr2O12 Nanowire Upgrading Polyethylene Oxide (PEO) Composite Electrolyte and PEO Cathode Binder. Adv. Funct. Mater. *29*, 1805301. https://doi.org/10.1002/adfm.201805301.

67. Liu, L., Chu, L., Jiang, B., and Li, M. (2019). Li1.4Al0.4Ti1.6(PO4)3 nanoparticle-reinforced solid polymer electrolytes for all-solid-state lithium batteries. Solid State Ion. *331*, 89–95. https://doi.org/10.1016/j.ssi.2019.01.007.

68. Fu, J., Yu, P., Zhang, N., Ren, G., Zheng, S., Huang, W., Long, X., Li, H., and Liu, X. (2019). In situ formation of a bifunctional interlayer enabled by a conversion reaction to initiatively prevent lithium dendrites in a garnet solid electrolyte. Energy Environ. Sci. *12*, 1404–1412. https://doi.org/10.1039/C8EE03390K.

69. Liu, Y., Su, H., Zhong, Y., Wang, X., Xia, X., Gu, C., and Tu, J. (2022). Revealing the Impact of Cl Substitution on the Crystallization Behavior and Interfacial Stability of Superionic Lithium

Argyrodites. Adv. Funct. Mater. *32*, 2207978. https://doi.org/10.1002/adfm.202207978.

70. Li, J., Liu, C., Miao, C., Kou, Z., Xiao, W., Liang, C., Zhou, H., Zhu, G., and Cao, J. (2022). Enhanced ionic conductivity and electrochemical stability of Indium doping Li1.3Al0.3Ti1.7(PO4)3 solid electrolytes for all-solid-state lithium-ion batteries. Ionics *28*, 63–72. https://doi.org/10.1007/s11581-021-04310-8.

71. Choi, Y., Kim, H., and Yoo, J. (2022). Regulating the Polarization of Lithium Metal Anode via Active and Inactive 3D Conductive Mesh Structure. Adv. Energy and Sustain. Res. *3*, 2200065. https://doi.org/10.1002/aesr.202200065.

72. Shao, A., Tang, X., Zhang, M., Bai, M., and Ma, Y. (2022). Challenges, Strategies, and Prospects of the Anode-Free Lithium Metal Batteries. Adv. Energy and Sustain. Res. *3*, 2100197. https://doi.org/10.1002/aesr.202100197.

73. Fairley, N., Fernandez, V., Richard-Plouet, M., Guillot-Deudon, C., Walton, J., Smith, E., Flahaut, D., Greiner, M., Biesinger, M., Tougaard, S., et al. (2021). Systematic and collaborative approach to problem solving using X-ray photoelectron spectroscopy. Applied Surface Science Advances *5*, 100112. https://doi.org/10.1016/j.apsadv.2021.100112.
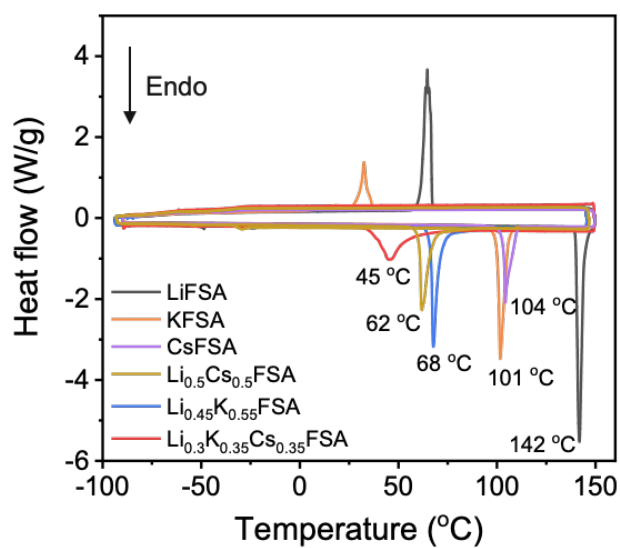
Supplemental information

Low melting alkali-based molten salt electrolytes

for solvent-free lithium-metal batteries

Minh Canh Vu, Priyadarshini Mirmira, Reginaldo J. Gomes, Peiyuan Ma, Emily S. Doyle, Hrishikesh S. Srinivasan, and Chibueze V. Amanchukwu

Figure S1. DSC thermograms. DSC thermograms of single salts of LiFSA, KFSA, CsFSA, binary mixture of Li$_{0.45}$K$_{0.55}$FSA (LiFSA:KFSA, 45:55 mol%) and ternary mixture of Li$_{0.3}$K$_{0.35}$Cs$_{0.35}$FSA (LiFSA:KFSA:CsFSA, 30:35:55 mol%).
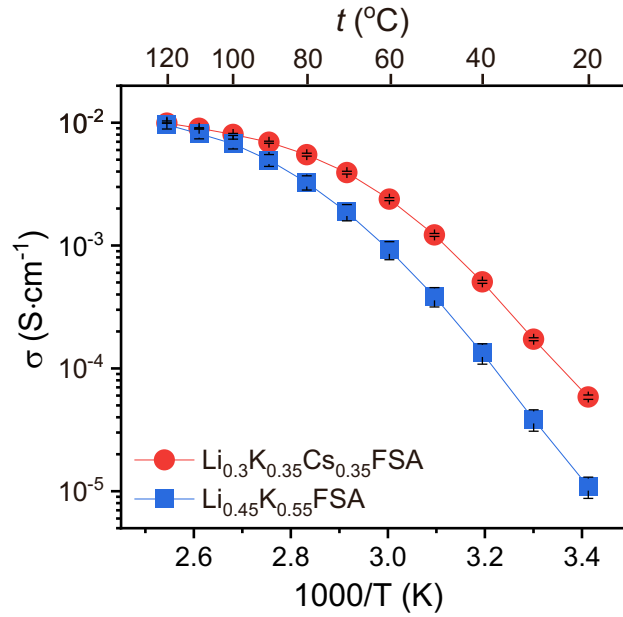
Figure S2. Ionic conductivity. Ionic conductivities of the binary $Li_{0.45}K_{0.55}FSA$ and ternary $Li_{0.3}K_{0.35}Cs_{0.35}FSA$ molten salts as a function of temperature with Vogel−Tammann−Fulcher calculation by the following equation[S1]

$$\sigma = Ae^{\left(-\frac{E_a}{R(T-T_0)}\right)}$$

where A, the prefactor, related to the effects of charge carrier concentration, and E_a, activation energy, related to segmental motion, on overall conductivity, σ, at a given temperature, T. T_0 in this equation is referred to as the Vogel temperature, which taken 50 °C below the glass transition temperature. The glass transition temperatures of binary $Li_{0.45}K_{0.55}FSA$ and ternary $Li_{0.3}K_{0.35}Cs_{0.35}FSA$ salts are -25.5 °C and -24.3 °C, respectively, which were collected from DSC profiles.
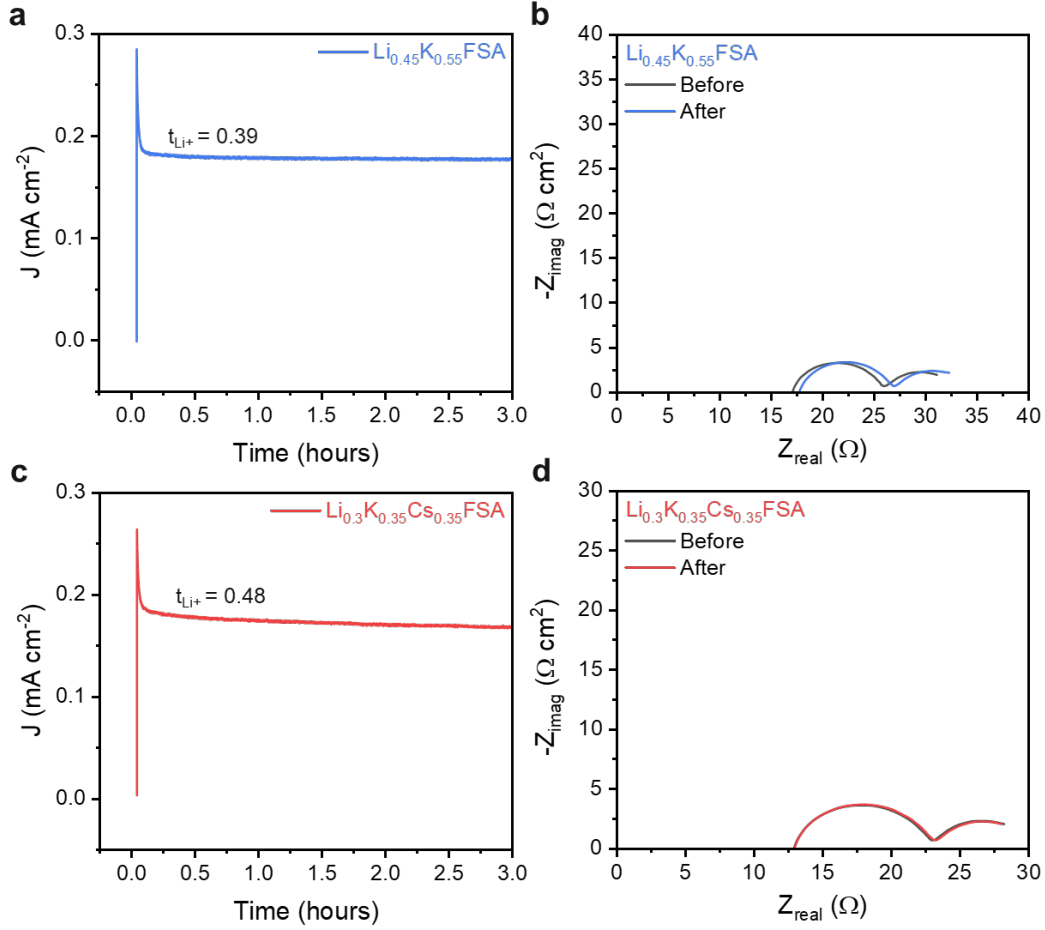
Figure S3. Lithium transference number (LTN) measurements at 80 °C. (a,c) Potentiostatic polarization (10 mV) curves of Li‖Li cells using the binary $Li_{0.45}K_{0.55}FSA$ and ternary $Li_{0.3}K_{0.35}Cs_{0.35}FSA$ molten salts electrolytes, respectively. (b, d) Electrochemical impedance spectra of Li‖Li cells using the binary $Li_{0.45}K_{0.55}FSA$ and ternary $Li_{0.3}K_{0.35}Cs_{0.35}FSA$ molten salts electrolytes before and after potentiostatic polarization measurements, respectively. The transference number was calculated according to the following equation[S2]:

$$t_{Li^+} = \frac{i_s(\Delta V - i_0 R_0)}{i_0(\Delta V - i_s R_s)}$$

The cells were polarized at a potential ΔV of 10 mV, the initial (i_0) and steady state (i_s) currents were measured. Impedance was also measured before (R_0) and after (R_s) polarization.
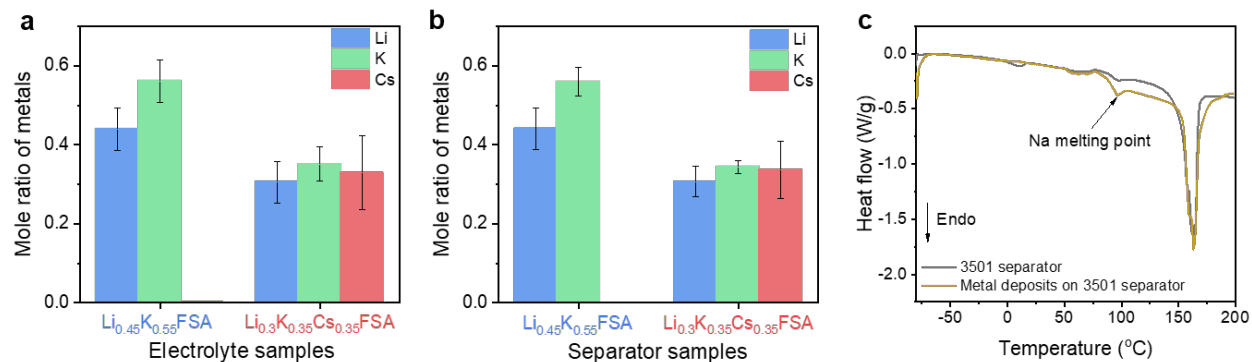
Figure S4. Metal compositions in molten salts from ICP-MS measurements. (a) Binary $Li_{0.45}K_{0.55}FSA$ molten salt and ternary $Li_{0.3}K_{0.35}Cs_{0.35}FSA$ molten salt as prepared. (b) Binary $Li_{0.45}K_{0.55}FSA$ and ternary $Li_{0.3}K_{0.35}Cs_{0.35}FSA$ molten salt electrolytes on the separator of the Li||Cu cells after metal deposition on copper electrode experiments.(c) DSC profiles of 3501 separator and the metal deposits on 3501 separator of the Li||Cu cells after metal deposition on copper electrode experiments
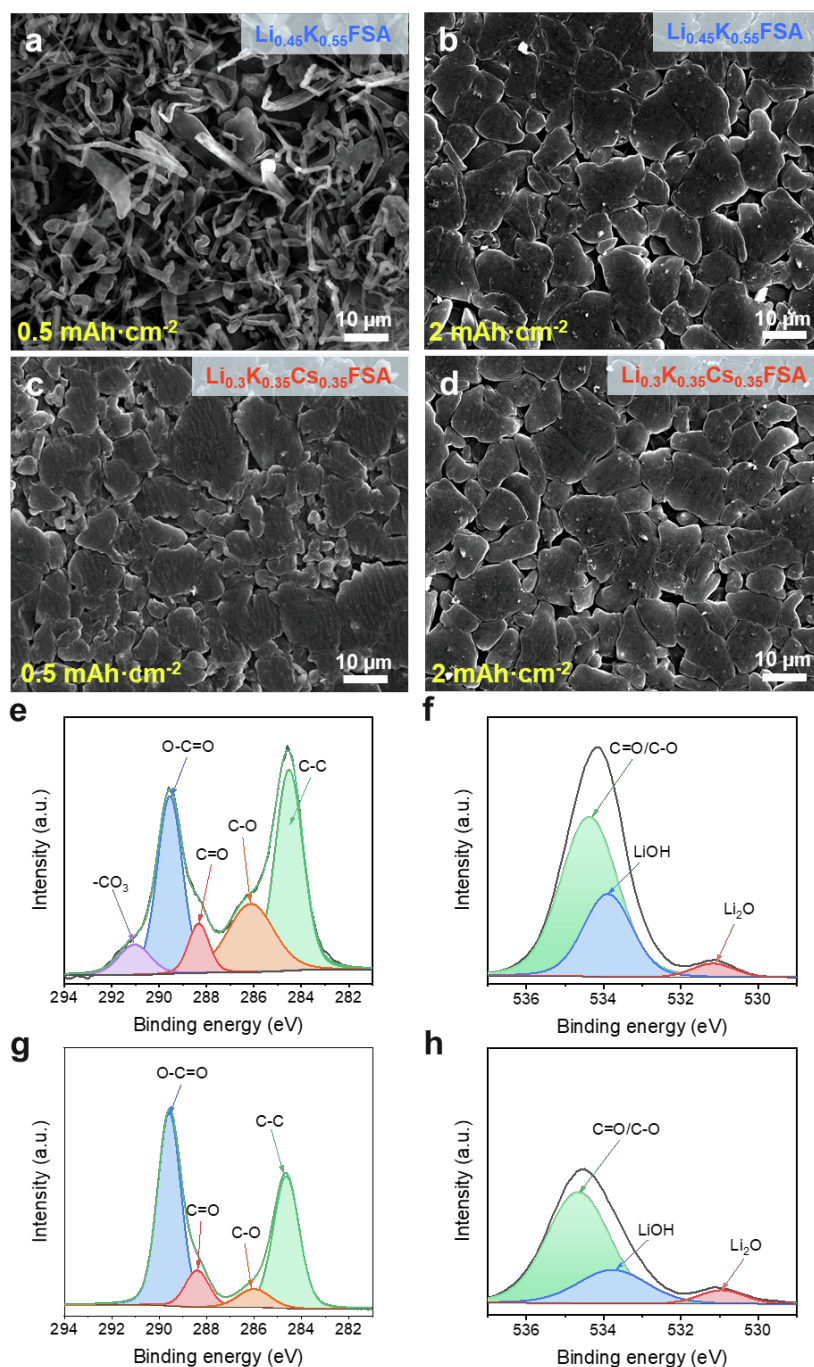
Figure S5. SEM images of metal deposition on copper electrodes at 0.5 mA cm^{-2} using molten salts electrolytes at different capacities. (a, b) Binary Li$_{0.45}$K$_{0.55}$FSA molten salt electrolytes at capacities of 0.5 mAh cm^{-2} and 2 mAh cm^{-2}, respectively. (c, d) Ternary Li$_{0.3}$K$_{0.35}$Cs$_{0.35}$FSA molten salt electrolytes at capacities of 0.5 mAh cm^{-2} and 2 mAh cm^{-2}, respectively. Deconvoluted XPS spectra of (**e**) C 1s, and (**f**) O 1s of Li surface in Li||Cu cells using 1M LiFSA/Pyr$_{14}$FSA electrolyte after 10 cycles and (**g**) C 1s, and (**h**) O 1s of Li surface in Li||Cu cells using Li$_{0.30}$K$_{0.35}$Cs$_{0.35}$FSA molten salt electrolyte after 10 cycles, respectively. a.u. = arbitrary units.
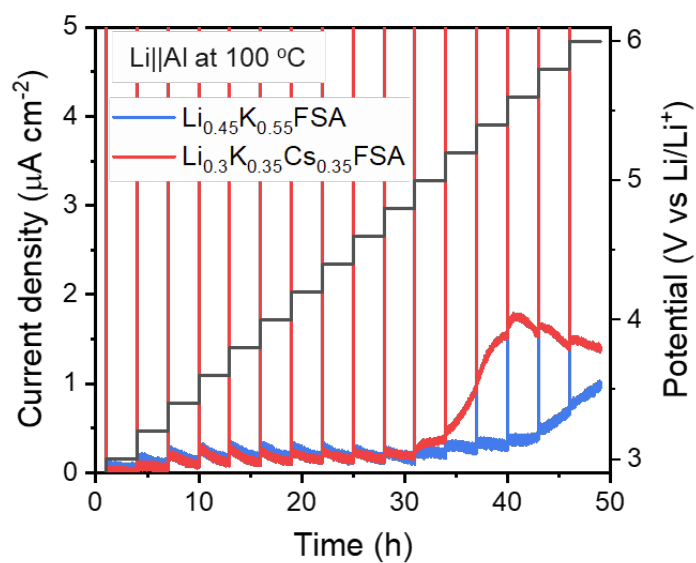
Figure S6. Potentiostatic holds in the voltage range of 3-6 V with a 0.2V interval in Li||Al cells using the binary $Li_{0.45}K_{0.55}FSA$ (blue line) and ternary $Li_{0.3}K_{0.35}Cs_{0.35}FSA$ (red line) molten salts electrolytes at 100 °C.
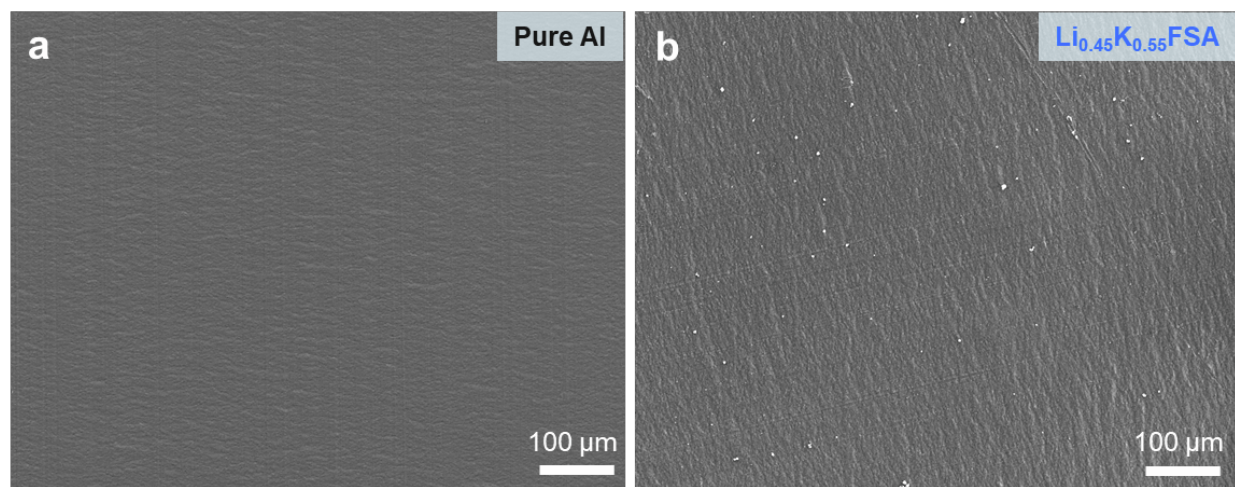

Figure S7. SEM images. (a) bare Al surface. (b) Al electrode surface after holding the Li||Al cells at the voltage of 5.5 V at 80 °C for 3 days using the binary $Li_{0.45}K_{0.55}FSA$ molten salt electrolytes.
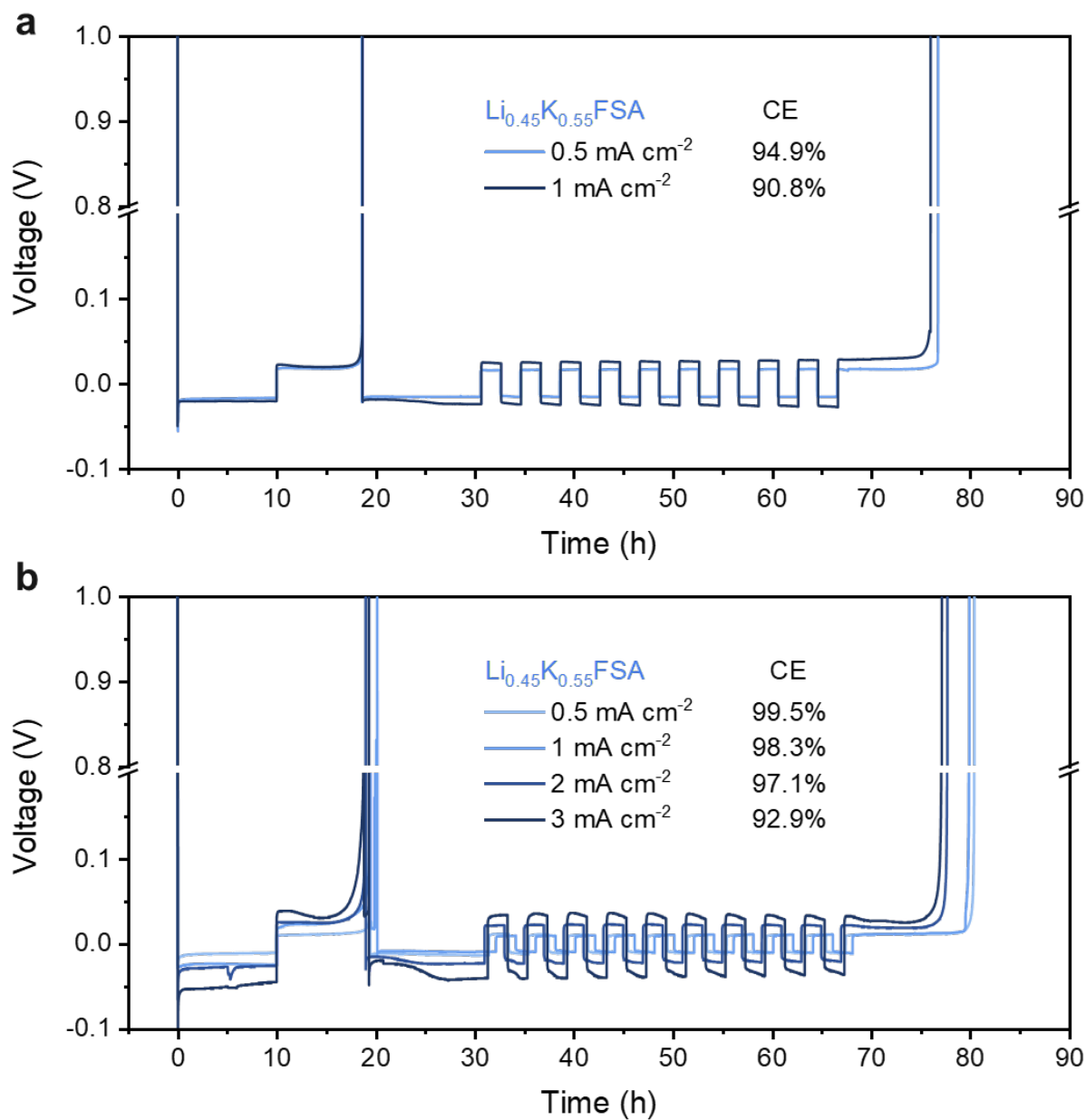
Figure S8. Coulombic efficiency (CE) measurements in Li||Cu cells at current densities of 0.5 mA cm^{-2}, 1 mA cm^{-2}, 2 mA cm^{-2}, and 3 mA cm^{-2} with 1 h of stripping/plating for 10 cycles using the Li$_{0.45}$K$_{0.55}$FSA electrolyte at various temperatures (a) 80 °C and (b) 100 °C.
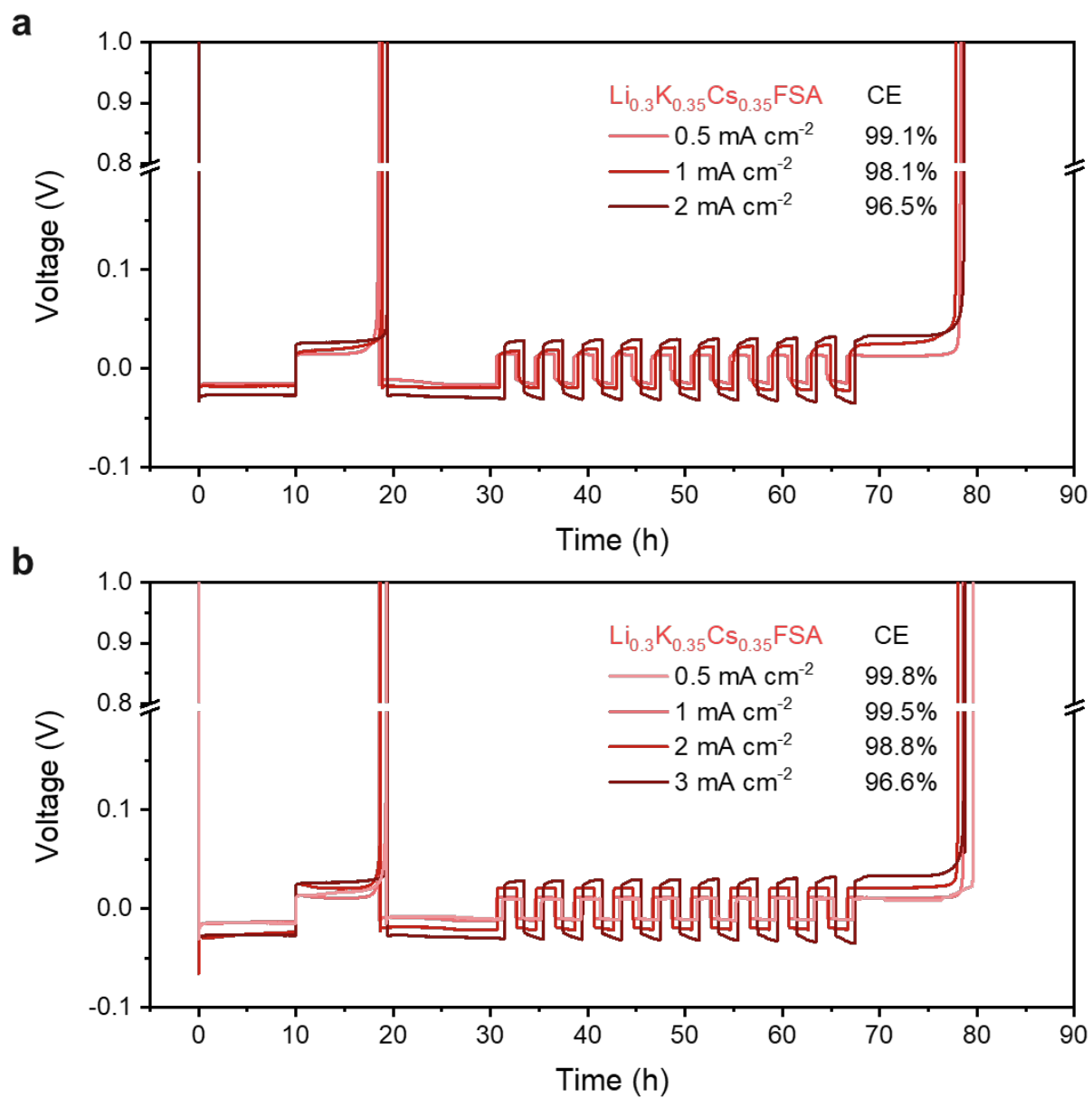
Figure S9. Coulombic efficiency (CE) measurements in Li||Cu cells at current densities of 0.5 mA cm^{-2}, 1 mA cm^{-2}, 2 mA cm^{-2}, and 3 mA cm^{-2} with 1 h of stripping/plating for 10 cycles using the Li$_{0.3}$K$_{0.35}$Cs$_{0.35}$FSA electrolyte at various temperatures. (a) 80 °C and (b) 100 °C.
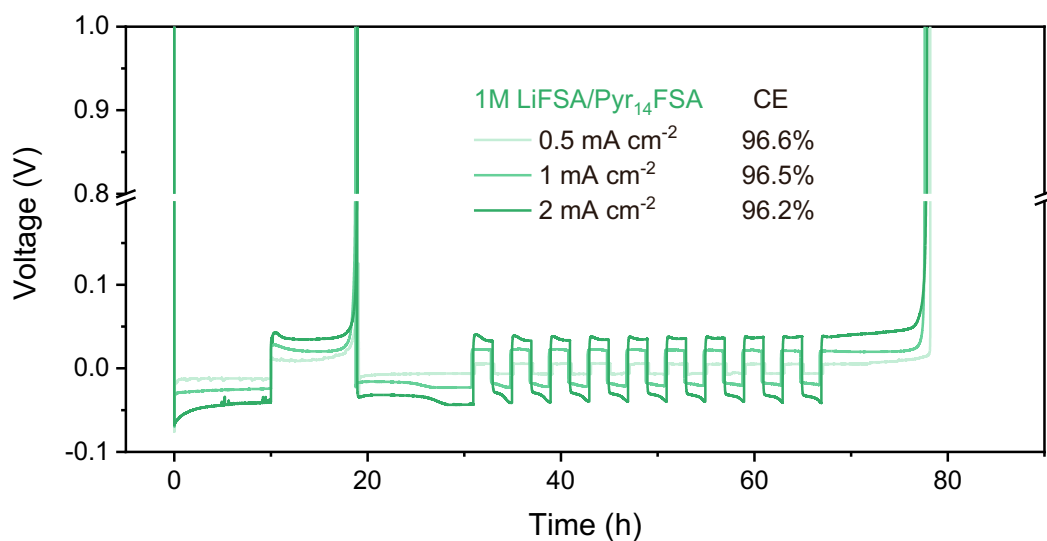
Figure S10. Coulombic efficiency (CE) measurements in Li||Cu cells at a current densities of 0.5 mA cm^{-2} to 1 mAh cm^{-2}, and 1 mA cm^{-2} to 2 mAh cm^{-2}, and 2 mA cm^{-2} to 4 mAh cm^{-2} using the 1M LiFSA/Pyr$_{14}$FSA ionic liquid electrolytes at 80 °C.
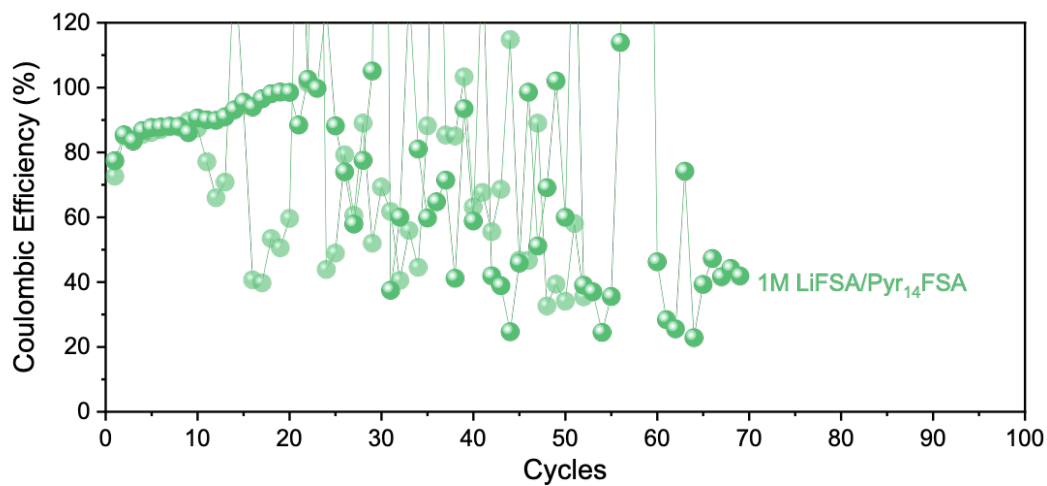

Figure S11. Li||Cu cells cycling at a current density of 0.5 mA cm^{-2} for 1 mAh cm^{-2} using the 1M LiFSA/Pyr$_{14}$FSA ionic liquid electrolytes at 80 °C.
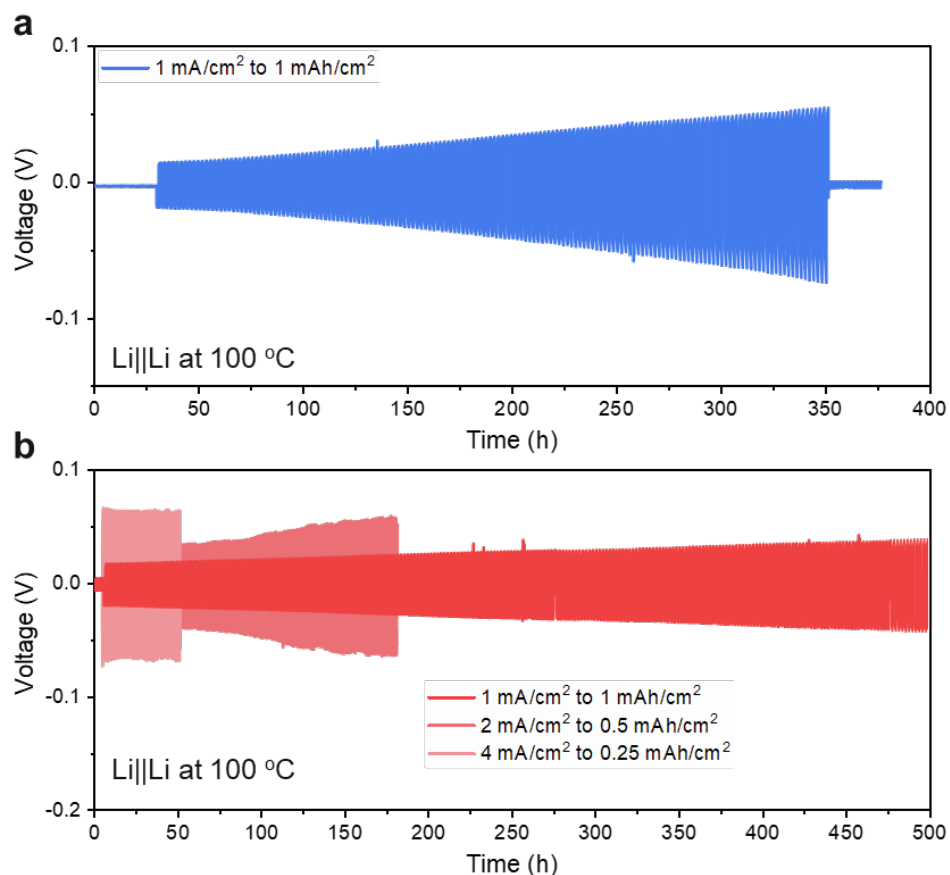
Figure S12. Li||Li cells cycling at 100 °C using different molten salt electrolytes. (a) Binary $Li_{0.45}K_{0.55}FSA$ molten salt at a current density of 1 mA cm^{-2} to 1 mAh cm^{-2}. (b) Ternary $Li_{0.3}K_{0.35}Cs_{0.35}FSA$ molten salt at different current densities and capacities.
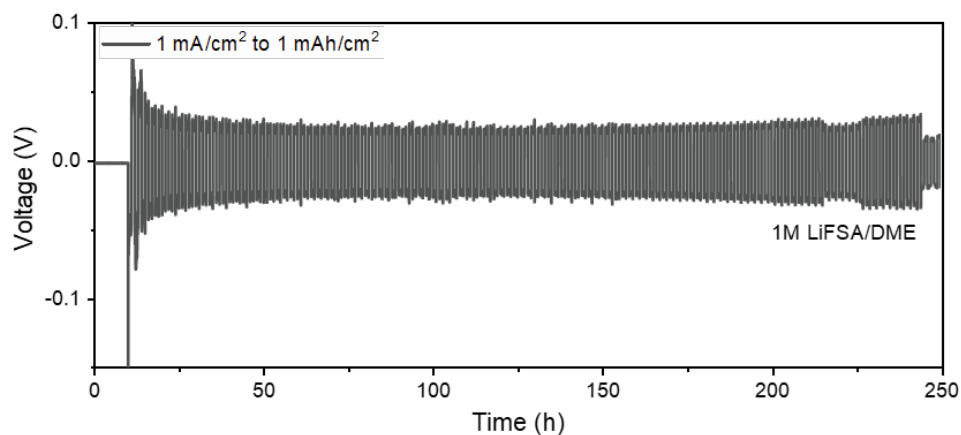
Figure S13. Li||Li cells cycling at 20 °C using 1M LiFSA/DME electrolyte at a current density of 1 mA cm^{-2} to 1 mAh cm^{-2}.
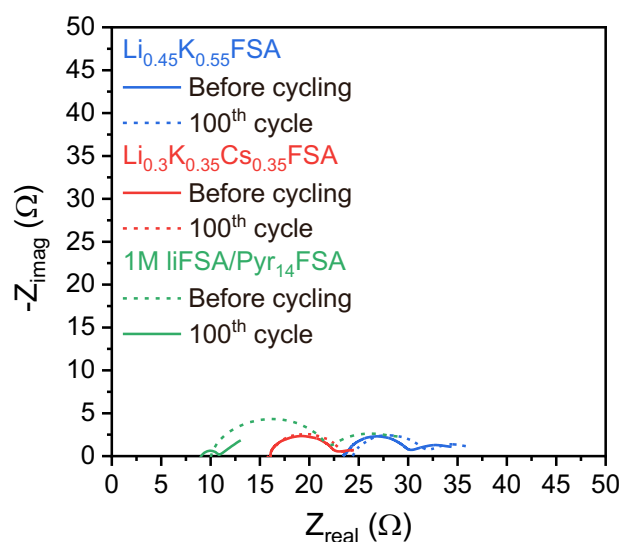
Figure S14. EIS of the Li||Li cells using molten salt and IL electrolytes before and after 100 cycles.
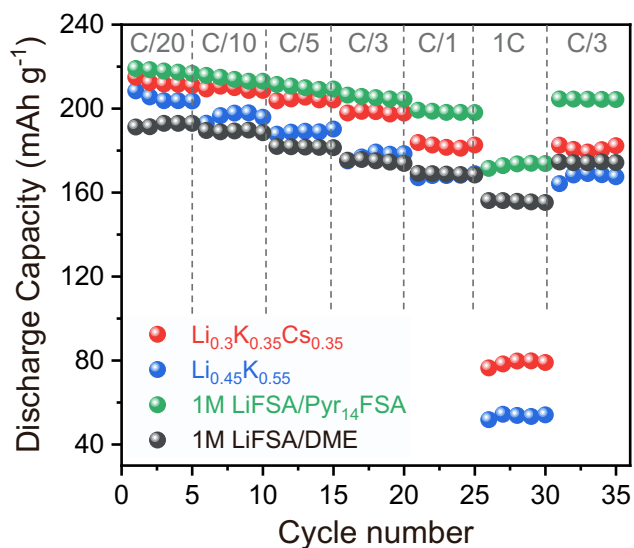
Figure S15. Galvanostatic discharge capacities of Li (500 μm)||NMC811 cells cycling using different electrolytes at different C-rates (5 cycles for each C-rates) respectively. 1C equals to 1.88 mA cm^{-2}. Cells using molten salts electrolytes and ionic liquid electrolytes were cycled at 80 °C while 1M LiFSA/DME cells were cycled at 20 °C.
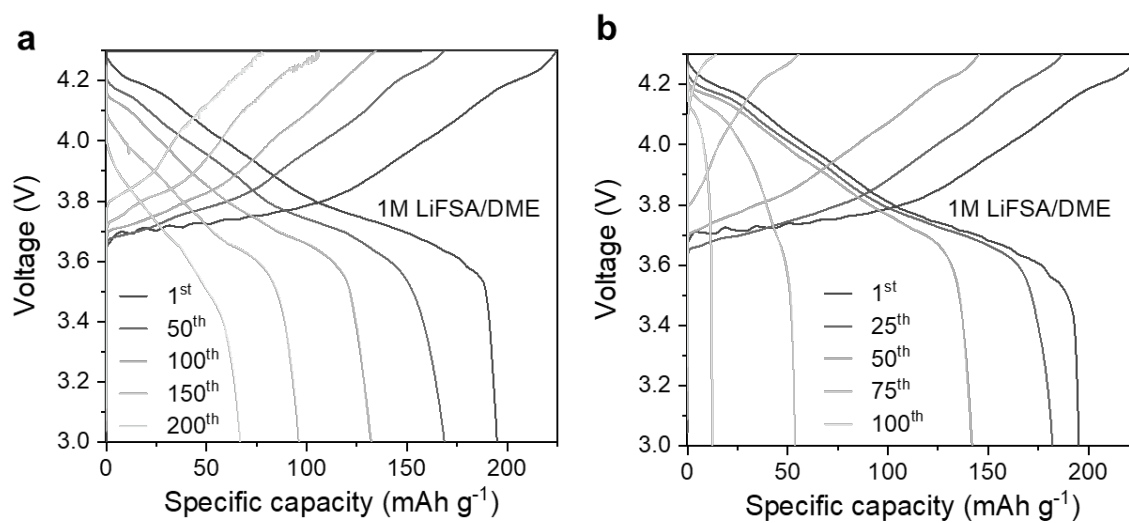
Figure S16. Selected voltage profiles of (a) Li||NMC811 cells, (b) Thin Li||NMC811 cells cycled a constant discharge rate of C/3 (after 3 formation cycles at C/20) using 1M LiFSA/DME at 20 °C.
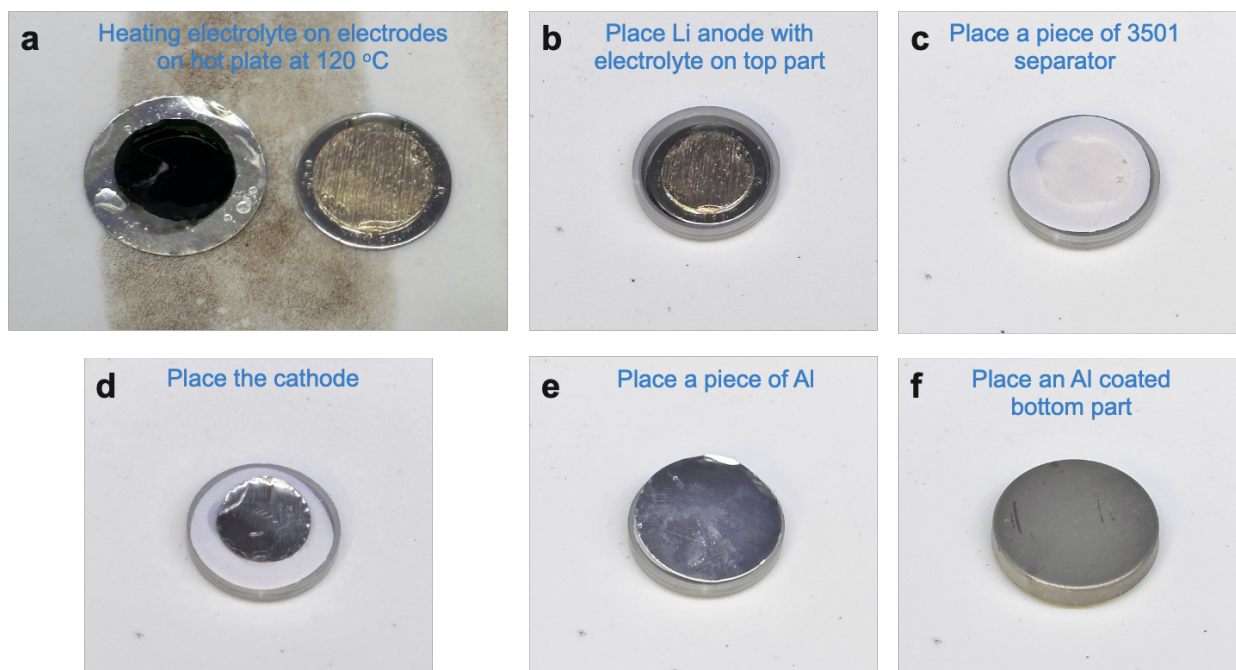
Figure S17. Steps of cell assembly process. (a) NMC811 cathode and Li metal anode on a spacer electrodes were placed on a surface of the hot plate at 120 °C. 100 mg of electrolytes was loaded on the top of electrodes and heated for 5 min to melt the electrolyte. (b) Li anode with melted electrolyte was placed on the top part of the cell, a spring and a spacer. (c) A piece of separator was placed on Li anode side, the electrolyte was penetrated through the separator. (d) The cathode with melted electrolytes was placed on the separator. (e) A piece of Al disk was placed on the cathode. (f) An Al coated bottom part was placed. After that the cell was transferred to the small antechamber for vacuuming and pressed at 700 MPa using the automatic coin cell crimper (TOB New Energy).

Table S1. A comparison of conventional electrolytes (e.g., 1M LiFSA/DME), high concentration electrolyte (e.g., 4M LiFSA/DME), organic ionic liquid electrolytes (1M LiFSA/Pyr$_{14}$FSA), and solvent-free molten salt (Li$_{0.30}$K$_{0.35}$Cs$_{0.35}$FSA) electrolytes. Note that the properties of liquid electrolytes and IL electrolytes were measured at room temperature while that of the molten salt electrolytes at 80 °C.

Properties	CLE 1M LiFSA/DME	HCE 4M LiFSA/DME	ILE 1M LiFSA/Pyr14FSA	SME Li$_{0.3}$K$_{0.35}$Cs$_{0.35}$FSA
Non-volatility	X	X	√	√
Thermal stability	X	X	√	√
σ (>2 mS/cm)	√	√	√	√
Li transfer number (>0.4)	~	√	X	√
Coulombic efficiency (>99%)	X	~	X	√
Al^0 stability (≥5.5 V)	X	√	~	√

CLE: conventional liquid electrolytes, HCE: high concentration electrolytes, ILE: ionic liquid electrolytes, SME: solvent-free molten salts electrolytes.

Table S2. A comparison of polymer electrolytes (PE), inorganic solid-sate electrolytes (ISSE) and solvent-free molten salt ($Li_{0.30}K_{0.35}Cs_{0.35}FSA$) electrolytes. Note that the properties of the PE and ISSE were measured at 60 °C while that of the molten salt electrolytes at 80 °C.

Properties	PE PEO	ISSE LPS	SME $Li_{0.3}K_{0.35}Cs_{0.35}FSA$
Conductivity (>2 mS/cm)	X	~	√
Li transfer number (>0.4)	X	√	√
Al^0 stability (≥5.5 V)	X	√	√
Coulombic efficiency (>99 %)	X	X	√
Low overpotential	~	X	√
High rates (>2 mA/cm^2)	X	X	√

PE: polymer electrolytes, ISSE: inorganic solid-state electrolytes.

Table S3. Comparison of full cell Li metal battery performance.

Electrolyte	Cathode	Current density	Capacity Retention
LiFSA in 1.2 DME (molar ratio)[S3]	NMC811 (4.4 V)	Charge = 0.5 mA cm^{-2} Discharge = 1.5 mA cm^{-2}	83% after 200 cycles
LiFSA in 1.2DME–3TTE (molar ratio)[S3]	NMC811 (4.4 V)		90% after 200 cycles
3.2 M LiFSA in TEP[S4]	NMC622 (4.4 V)	Charge ≈ 0.5 mA cm^{-2} Discharge = 1.6 mA cm^{-2}	64% after 200 cycles
LiFSA in 2.2DMC–3TTE (molar ratio)[S5]	NMC811 (4.4 V)	Charge = 0.5 mA cm^{-2} Discharge = 0.5 mA cm^{-2}	75% after 200 cycles
LiFSA in 3TMS–3TTE (molar ratio)[S5]	NMC811 (4.4 V)	Charge = 0.5 mA cm^{-2} Discharge = 0.5 mA cm^{-2}	68% after 200 cycles
LiFSA in 3TMS (molar ratio)[S6]	NMC333 (4.3 V)	Charge = 0.5 mA cm^{-2} Discharge = 0.5 mA cm^{-2}	86% after 200 cycles
5.5 M LiFSA in DMC[S7]	NMC333 (4.3 V)	Charge = 2.0 mA cm^{-2} Discharge = 2.0 mA cm^{-2}	87% after 200 cycles
3.0 M LiTFSI in DME[S8]	NMC333 (4.3 V)	Charge = 0.57 mA cm^{-2} Discharge = 1.7 mA cm^{-2}	82% after 200 cycles
4.0 M LiODFB in DME[S8]	NMC333 (4.3 V)	Charge = 0.57 mA cm^{-2} Discharge = 1.7 mA cm^{-2}	56% after 200 cycles
4.0 M LiFSA in DME[S9]	NMC811 (4.4 V)	Charge = 2.5 mA cm^{-2} Discharge = 2.5 mA cm^{-2}	71% (170 cycles)
This work Li$_{0.3}$K$_{0.35}$Cs$_{0.35}$FSA molten salt, Solventless, Nonflammable, Nonvolatile	NMC811 (4.3 V)	Charge = 0.67 mA cm^{-2} Discharge = 0.67 mA cm^{-2}	75% after 200 cycles, C/3

Table S4. Comparison of anode-free Li metal battery performance.

Electrolyte	Cell Condition	Capacity Retention and C rate
4 M LiFSA in DME[S10]	Cu||LFP coin cell, 1.71 mAh cm^{-2}	60% after 50 cycles, C/8
1 M LiTFSI + 2 M LiFSI + 3 wt% LiNO$_3$ in DME/DOL[S11]	Cu||LFP coin cell, 0.85 mAh cm^{-2}	39% after 100 cycles
7 M LiFSA in FEC[S12]	Cu||LNMO coin cell, 1.43 mAh cm^{-2}	54% after 50 cycles
2 M LiPF$_6$ in EC/DEC + 50% FEC [S13]	Cu||NMC111 coin cell, 1.6 mAh cm^{-2}	40% after 50 cycles, C/8
1 M LiPF$_6$ in FEC/FEMC/HFE[S14]	Cu||NMC811 coin cell, 2.0 mAh cm^{-2}	50% after 30 cycles, C/4
1M LiFSA in 1.2DME-3TTE[S15]	Cu||NMC811 coin cell, 4.2 mAh cm^{-2}	77% after 70 cycles, C/3
1 M LiPF$_6$ + 1% LiPO$_2$F$_2$ in FEC/TTE/EMC/MA[S16]	Cu||NMC811 coin cell, 0.5 mA cm^{-2}	51% after 40 cycles
2 M LiFSA + 2M LiNO$_3$ in DME[S17]	Cu||NMC811 coin cell, 2 mAh cm^{-2}	50% after 100 cycles
1 mol LiFSA in 1 mol P$_{1222}$FSI[S18]	Cu||NMC622 coin cell, 3.5 mAh cm^{-2}	33% after 100 cycles, C/2
This work Li$_{0.3}$K$_{0.35}$Cs$_{0.35}$FSA molten salt Solventless, Nonflammable, Nonvolatile	Cu||NMC811 coin cells, 1.66 mAh cm^{-2}	40% after 100 cycles, C/3

References

[S1]. Diederichsen, K.M., Buss, H.G., and McCloskey, B.D. (2017). The Compensation Effect in the Vogel-Tammann-Fulcher (VTF) Equation for Polymer-Based Electrolytes. Macromolecules *50*, 3831–3840. 10.1021/acs.macromol.7b00423.

[S2]. Zugmann, S., Fleischmann, M., Amereller, M., Gschwind, R.M., Wiemhöfer, H.D., and Gores, H.J. (2011). Measurement of transference numbers for lithium ion electrolytes via four different methods, a comparative study. Electrochim Acta *56*, 3926–3933. 10.1016/j.electacta.2011.02.025.

[S3]. Ren, X., Zou, L., Cao, X., Engelhard, M.H., Liu, W., Burton, S.D., Lee, H., Niu, C., Matthews, B.E., Zhu, Z., et al. (2019). Enabling High-Voltage Lithium-Metal Batteries under Practical Conditions. Joule *3*, 1662–1676. 10.1016/j.joule.2019.05.006.

[S4]. Chen, S., Zheng, J., Yu, L., Ren, X., Engelhard, M.H., Niu, C., Lee, H., Xu, W., Xiao, J., Liu, J., et al. (2018). High-Efficiency Lithium Metal Batteries with Fire-Retardant Electrolytes. Joule *2*, 1548–1558. 10.1016/j.joule.2018.05.002.

[S5]. Ren, X., Gao, P., Zou, L., Jiao, S., Cao, X., Zhang, X., Jia, H., Engelhard, M.H., Matthews, B.E., Wu, H., et al. (2020). Role of inner solvation sheath within salt–solvent complexes in tailoring electrode/electrolyte interphases for lithium metal batteries. Proc Natl Acad Sci USA *117*, 28603–28613. 10.1073/pnas.2010852117.

[S6]. Ren, X., Chen, S., Lee, H., Mei, D., Engelhard, M.H., Burton, S.D., Zhao, W., Zheng, J., Li, Q., Ding, M.S., et al. (2018). Localized High-Concentration Sulfone Electrolytes for High-Efficiency Lithium-Metal Batteries. Chem *4*, 1877–1892. 10.1016/j.chempr.2018.05.002.

[S7]. Chen, S., Zheng, J., Mei, D., Han, K.S., Engelhard, M.H., Zhao, W., Xu, W., Liu, J., and Zhang, J.G. (2018). High-Voltage Lithium-Metal Batteries Enabled by Localized High-Concentration Electrolytes. Advanced Materials *30*, 1706102. 10.1002/adma.201706102.

[S8]. Ren, X., Zou, L., Jiao, S., Mei, D., Engelhard, M.H., Li, Q., Lee, H., Niu, C., Adams, B.D., Wang, C., et al. (2019). High-concentration ether electrolytes for stable high-voltage lithium metal batteries. ACS Energy Lett *4*, 896–902. 10.1021/acsenergylett.9b00381.

[S9]. Pham, T.D., Faheem, A. Bin, Kim, J., Oh, H.M., Lee, K.-K., Pham, T.D., Faheem, A. Bin, Kim, J., Lee, K.-K., and Oh, H.M. (2022). Practical High-Voltage Lithium Metal Batteries Enabled by Tuning the Solvation Structure in Weakly Solvating Electrolyte. Small *18*, 2107492. 10.1002/smll.202107492.

[S10]. Qian, J., Adams, B.D., Zheng, J., Xu, W., Henderson, W.A., Wang, J., Bowden, M.E., Xu, S., Hu, J., Zhang, J.-G., et al. (2016). Anode-Free Rechargeable Lithium Metal Batteries. Adv Funct Mater *26*, 7094–7102. 10.1002/adfm.201602353.

[S11]. Qiu, F., Li, X., Deng, H., Wang, D., Mu, X., He, P., Zhou, H., Qiu, F., Wang, D., Mu, X., et al. (2019). A Concentrated Ternary-Salts Electrolyte for High Reversible Li Metal Battery with Slight Excess Li. Adv Energy Mater *9*, 1803372. 10.1002/aenm.201803372.

[S12]. Suo, L., Xue, W., Gobet, M., Greenbaum, S.G., Wang, C., Chen, Y., Yang, W., Li, Y., and Li, J. (2018). Fluorine-donating electrolytes enable highly reversible 5-V-class Li metal batteries. Proc Natl Acad Sci USA *115*, 1156–1161. 10.1073/pnas.1712895115.

[S13]. Hagos, T.T., Thirumalraj, B., Huang, C.J., Abrha, L.H., Hagos, T.M., Berhe, G.B., Bezabh, H.K., Cherng, J., Chiu, S.F., Su, W.N., et al. (2019). Locally Concentrated $LiPF_6$ in a Carbonate-Based Electrolyte with Fluoroethylene Carbonate as a Diluent for Anode-Free Lithium Metal Batteries. ACS Appl Mater Interfaces *11*, 9955–9963. 10.1021/acsami.8b21052.

[S14]. Fan, X., Chen, L., Borodin, O., Ji, X., Chen, J., Hou, S., Deng, T., Zheng, J., Yang, C., Liou, S.C., et al. (2018). Non-flammable electrolyte enables Li-metal batteries with aggressive cathode chemistries. Nature Nanotechnology *13*, 715–722. 10.1038/s41565-018-0183-2.

[S15]. Ren, X., Zou, L., Cao, X., Engelhard, M.H., Liu, W., Burton, S.D., Lee, H., Niu, C., Matthews, B.E., Zhu, Z., et al. (2019). Enabling High-Voltage Lithium-Metal Batteries under Practical Conditions. Joule *3*, 1662–1676. 10.1016/j.joule.2019.05.006.

[S16]. Hotasi, B.T., Hagos, T.M., Huang, C.J., Jiang, S.K., Jote, B.A., Shitaw, K.N., Bezabh, H.K., Wang, C.H., Su, W.N., Wu, S.H., et al. (2022). Developing ester-based fluorinated electrolyte with LiPO2F2 as an additive for high-rate and thermally robust anode-free lithium metal battery. J Power Sources *548*, 232047. 10.1016/j.jpowsour.2022.232047.

[S17]. Kang, D.W., Moon, J., Choi, H.Y., Shin, H.C., and Kim, B.G. (2021). Stable cycling and uniform lithium deposition in anode-free lithium-metal batteries enabled by a high-concentration dual-salt electrolyte with high LiNO3 content. J Power Sources *490*, 229504. 10.1016/j.jpowsour.2021.229504.

[S18]. Pathirana, T., Kerr, R., Forsyth, M., and Howlett, P.C. (2021). Application of super-concentrated phosphonium based ionic liquid electrolyte for anode-free lithium metal batteries. Sustain Energy Fuels *5*, 4141–4152. 10.1039/D1SE00724F.